UNIVERSITY OF CALIFORNIA SAN DIEGO

Analysis of sea surface scatter in the time-varying impulse response

A dissertation submitted in partial satisfaction of the
requirements for the degree
Doctor of Philosophy

in

Oceanography

by

Edward L. Richards

Committee in charge:

Professor William S. Hodgkiss, Co-Chair
Professor Hee-Chun Song, Co-Chair
Professor Michael J. Buckingham
Professor William A. Kuperman
Professor Geno Pawlak
Professor Peter Shearer

2020

The dissertation of Edward L. Richards is approved, and it is acceptable in quality and form for publication on microfilm and electronically:

_____

_____

_____

_____

_____
Co-Chair

_____
Co-Chair

University of California San Diego

2020

DEDICATION

To G-Mop and Fred, who always welcome me with open arms to the Nest.

TABLE OF CONTENTS

LIST OF FIGURES

ACKNOWLEDGEMENTS

I will always remember my time at Scripps Institution of Oceanography (SIO) fondly because I met so many remarkably people over the course of my PhD. My Applied Ocean Science cohort stuck together through our class work and made this time much more than simply learning subject matter. The other students at SIO, both the ones who were there when I arrived and the ones who showed up once I was here, made the experience the most humbling and richest of my life. There are too many to mention everyone by name. However, I will make an exception for my wife, Jasmeet, who was the best thing that I discovered in graduate school.

The work presented here would not exist without the help of numerous collaborators. I would first like to thank my committe members, who taught me most of what I know about the field of ocean acoustics, and then helped me put my work into a larger scientific context. Additionally, I gained significant support throughout my research from friendly discussion related to this research with Youngmin Choo, Eric Thorsos, Myrl Hendershott, and Stefan Llewellyn Smith.

The staff members at SIO helped me in many ways in my time as a student, probably much more than I know. In particular, I want to thank BethAnn Clausen, who was always willing to help me resolve whatever bureacratic confusion I found myself in. Gilbert Bretado has been a great resorce as well, both in his offical capacity and when he organized student mixers or outreach programs. I also want to thank Maureen McGreevy, who helped me to develop a popular outreach project with City College robotics students.

Finally, I want to acknowledge my family, both near and far, without whom none of this would have been possible.

Chapter 2, in full, is a reprint of the material as it appears in the Journal of the Acoustical Society of America 2018, authored by; Edward L. Richards, H. C. Song and W. S. Hodgkiss. The dissertation/thesis author was the primary investigator and author of this paper. This research was supported by the Office of Naval Research under grants N00014-14-1-0459 and N00014-16-1-

2476 and N00014-18-1-2123.

Chapter 3, in full, is a reprint of a rejected submission to the Journal of the Acoustical Society of America 2019, authored by Edward L. Richards, H. C. Song and W. S. Hodgkiss. The dissertation/thesis author was the primary investigator and author of this paper. While this work was not considered sufficently novel for publication as is, it represented a signifcant research effort and is included as a thesis chapter. This research was supported by the Office of Naval Research under grant N00014-18-1-2123.

Chapter 4, in full, has been submitted for publication in the Journal of the Acoustical Society of Americal as an express letter, authored by Edward L. Richards, H. C. Song and W. S. Hodgkiss. The dissertation/thesis author was the primary investigator and author of this paper. This research was supported by the Office of Naval Research under grant N00014-19-1-2635.

VITA

2011	Bachelor of Science in Ocean Engineering, University of Rhode Island
2013	Master of Science in Ocean Engineering, University of Rhode Island
2020	Doctor of Philosophy in Oceanography, University of California San Diego

PUBLICATIONS

Journals

Edward L. Richards, H. C. Song and W. S. Hodgkiss, "Acoustic scattering comparison of Kirchhoff approximation to Rayleigh-Fourier method for sinusoidal surface waves at low grazing angles", *The Journal of the Acoustical Society of America*, vol. 144, pp. 1269-1298, 2018.

Zhuqing Zang, E. L. Richards, H. C. Song and W. S. Hodgkiss, "Calibration of vertical array tilt using snapping shrimp sound", *The Journal of the Acoustical Society of America*, vol. 144, pp. 1203-1210, 2018.

Conferences

Edward L. Richards and Gopu Potty, "Acoustic interface treatment with an adjoint operator for linear range-dependent ocean index of refraction inversions," *Acoustical Society of America*, Montreal, Quebec, Canada, 2013.

Edward L. Richards, W. S. Hodgkiss and H.C. Song, "Modeling surface scatter in the channel impulse response with a Helmholtz-Kirchhoff integral," *Acoustical Society of America*, Honolulu, HI, 2016.

Edward L. Richards, W. S. Hodgkiss and H.C. Song, "Modelling broadband scatter from periodic sea surfaces," *Acoustical Society of America*, New Orleans, LA, 2017.

Edward L. Richards, Z. Q. Yuan, H.C. Song and W. S. Hodgkiss, "Vertical line array tilt revealed through snapping shrimp noise," *Acoustical Society of America*, Victoria, British Columbia, Canada, 2018.

Edward L. Richards, W. S. Hodgkiss and H.C. Song, "Limited duration integral equation method," *Acoustical Society of America*, San Diego, CA, 2019.

Miscellaneous

Edward L. Richards, "Effect of the Acoustic Environment on Adjoint Sound Speed Inversions," Master thesis, University of Rhode Island, 2013.

Edward L. Richards "Range dependent index of refraction inversion with the adjoint method using statistics from glider surveys," La Spezia: CMRE, 2013/06.

ABSTRACT OF THE DISSERTATION

Analysis of sea surface scatter in the time-varying impulse response

by

Edward L. Richards

Doctor of Philosophy in Oceanography

University of California San Diego, 2020

Professor William S. Hodgkiss, Co-Chair
Professor Hee-Chun Song, Co-Chair

In ocean environments, acoustics is the primary means of signal transmission, and sea surface waves can cause significant propagation variability. Reflections from the moving sea surface waves cause transient, and often simultaneous, acoustic arrivals. The motivation for this study is to better understand scattered arrivals, which complicate processing of acoustic signals in communication systems. Numerical methods are presented that improve modeling of acoustic scatter in estimates of the time-varying channel impulse response. These methods are both intended to improve prediction of surface scatter, and also to relate scatter arrivals to features on the sea surface. Complementary analysis of experimental measurements also relates

scatter observations to reflecting features on the sea surface. Taken together, these numerical and experimental analyses both show how surface waves lead to surface scatter, and also how scatter arrival observations can reveal properties of these surface waves.

Several numerical model methods, both approximate and exact, are used to calculate sea surface scatter. The approximate models are eigen-rays and the Kirchhoff approximation, and the exact models are the Rayleigh-Fourier method (RFM) and the limited duration integral equation method (DIEM). While the eigen-ray solution is often less accurate than the Kirchhoff approximation, it can be used to show the positions on the sea surface that serve as acoustic reflectors. The Kirchhoff approximation, in turn, often gives accurate results at close ranges but diverges significantly from the exact solution at moderate to long ranges. While the RFM was used to initially demonstrate these results, the DIEM method was developed as a more general method for exact calculations of surface scatter.

Experimental measurements of surface scatter are significantly more cluttered than predictions from the numerical models. This issue is addressed with Doppler sensitive probe signals, which enable resolving scatter arrivals with different Doppler shifts. The flat surface travel time demonstrates how the Doppler shift relates to both the position and velocity of each surface reflector. Doppler selective processing is then shown to select for surface reflectors from limited portions of the sea surface. These results improve the interpretation of scatter observations, and are intended to inform future studies that compare numerical results with experimental measurements.

Chapter 1

Introduction

Ocean acoustics has been used in numerous applications, including environmental surveys, fish stock assessment, anti-submarine warfare (ASW), and underwater wireless communication [1]. In many of these applications, acoustic signals replace electromagnetic signals in analogous systems such as radar, satellite altimetry and cellphone communications. Acoustic signals are especially useful in oceanographic research and applications because the ocean environment allows for sound propagation over long distances. By contrast, electromagnetic signals attenuate rapidly in the ocean, evidenced by the underwater light field becoming darker only a few meters below the surface. Consequently, acoustic signals are the only practical means of signal transmission over significant distances at sea [2].

The longest open-ocean acoustic transmissions have been done with relatively deep sources and receivers (*e.g.* the Heard island feasibility test [3]). These long-range transmissions utilize the deep sound channel, a refracting duct located approximately 1 km deep in most of the worlds oceans. In the deep sound channel, a significant portion of the acoustic energy propagates without interaction with either the surface or bottom ocean boundaries, and thus lower loss. This property of the channel contrasts other cases in which either or both of these boundaries cause significant signal loss. Such signal loss generally occurs because these boundaries scatter or attenuate signals interacting with them.

The commonly used phrase "one researchers noise is anothers signal", applies just as well when "scatter" is used instead of "noise". Scatter means both "to cause to separate widely" and "to cause to vanish". In many experimental settings, scatter from boundaries does cause acoustic signals to reduce in amplitude and eventually vanish, precluding the analysis of acoustic transmissions. However, when scattered signals are detectable and observed clearly, they generally contain information about widely separated events on the surface.

Work by Cox and Munk [4] on sea surface glitter, visible light scattered off the sea surface, was an early demonstration of how scattered signals can be used to study the ocean surface. Cox and Munk took aerial photographs of the suns reflection on the surface of the ocean and showed

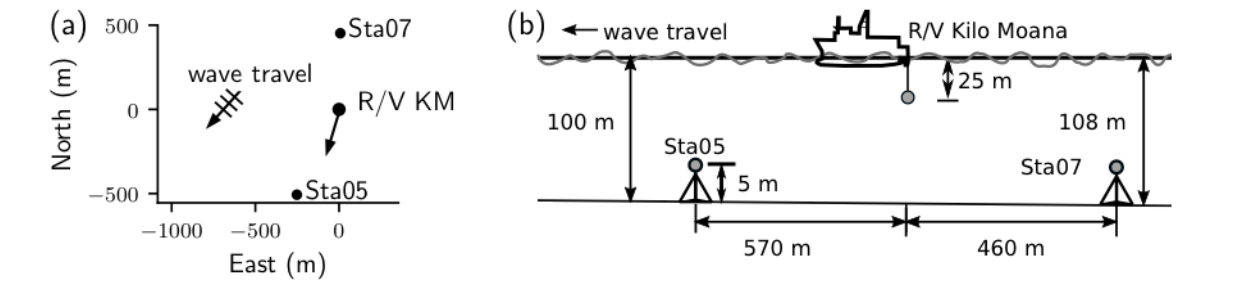

Figure 1.1: Experimental geometry of KAM11 tripod transmissions: (a) plan view and (b) side view.

how the spatial extent of the solar bright spot depended on local wind conditions. The results from this study have since been extended to measurements of wind speed across the open ocean by satellite using electromagnetic radiation.[5]

This study of acoustic scatter primarily is motivated by the application of acoustic communication.[6, 7] Acoustic communication is the underwater analog of cellphone and Wi-Fi communication, where acoustic, instead of electromagnetic, signals carry communication sequences between modems.[8] However, this analogy often is imperfect and electromagnetic wireless communication research cannot always be directly applied to acoustic communication. Instead, both experimental and numerical studies are necessary to address the physics unique to underwater acoustic communication.

An important part of underwater communication studies, like the Kauai Acomms MURI 2011 (KAM11) experiment discussed here, are repeated measurements of the underwater communication channel in a variety of environmental conditions. These measurements are made by the transmissions of specialized probe signals, which were sent between a number of different source and receiver stations over the course of the KAM11 experiment. Between the numerous components of the KAM11 experiment, the test setup shown in Fig. 1.1 specifically facilitated the study of surface scatter, [9] and is the motivation of this thesis. Like previous studies of this setup,[9, 10, 11] this thesis takes a deterministic approach to analyze the surface scatter, which is a relatively recent framework that works to describes discrete events in scatter observations.[6]

The deterministic approach is important because acoustic scatter is often episodic, with relatively rare but high amplitude arrivals, which are difficult to describe statistically.

The term deterministic scatter was introduced to first describe a short-range at-sea experiment that measured the sea surface profile simultaneously with acoustic channel measurements.[6] The sea-surface profile was used to model the received scatter arrivals, in many cases with high accuracy. Similar experiments were made in the surf zone [7] and in wave tanks [12, 13, 14] that focused on correlating acoustic scatter arrivals with specific reflecting features on the surface waves.

The KAM11 data represents an important extension of these deterministic scatter studies to longer-range transmissions, but it presents two additional challenges discussed here. First, the measurement of the sea-surface profile is challenging over longer ranges, and measurements made during the KAM11 instead characterized the ocean wave state statistically. Consequently, analysis of the KAM11 arrivals is largely performed in a qualitative manner by visually comparing observations to scatter from hypothetical sea-state realizations. Secondly, common approximations used to model acoustic scatter break down at longer ranges,[15] which require careful assessment before they can be used with confidence.

This thesis works to improve the analysis of KAM11 scatter, with the aim of extending the study of deterministic acoustic scatter to longer transmission ranges. The numerical modeling of surface scatter and the analysis of KAM11 experimental observations make up two distinct parts of this thesis. Chapters 2 and 3 present the numerical model results that improve the simulation of the surface scatter in communication transmission scenarios like that of KAM11. Chapter 4 presents a method that relates acoustic scatter arrivals to a position and velocity estimate of a surface reflector. Finally, Ch. 5 summarizes the major findings of each study, and suggests possible directions for future work.

1.1 Framework of observations and analysis

This section provides a brief overview of the theoretical framework used in this thesis to describe, model and measure surface scatter.

1.1.1 Channel impulse response

The time-evolving channel impulse response will be used here to characterize the acoustic propagation between the source and receiver and can be used to simulate the received signal for any specific transmission signal. A schematic of the channel impulse response for the KAM11 experiment appears in Fig. 1.2, modeled for an iso-speed environment with a flat, mirror-like, ocean surface and bottom.[2] This simple propagation environment has an analytic solution in which reflections from both top and bottom boundaries create arrivals that are delayed and scaled replicas of the transmitted signal. In the figure, only the first four arrivals are shown, although many additional paths exist with repeated interactions between the sea surface and ocean bottom.

The received signal is represented in Fig. 1.2 (b) as a series of the lollipops commonly used to show an impulse, or delta, function. The delta function is a generalized function of theoretically zero duration that cannot be realized physically.[16] This function is approximated experimentally using specialized probe signals and processing, discussed in Sec. 1.1.3. A received time series of any transmitted signal can be simulated using the impulse response by super-position. In super-position, each of the impulses shown in Fig. 1.2 (b) represents a scaled and delayed copy of the transmitted signal that is added together to create the simulated time series.

The complete duration of the impulse response typically is many milliseconds long. This means a significant period of silence is required between multiple transmissions, even if the original transmission was very short, for the receptions to not overlap. In an acoustic communication scenario where each symbol represents one to a few bits of information, this

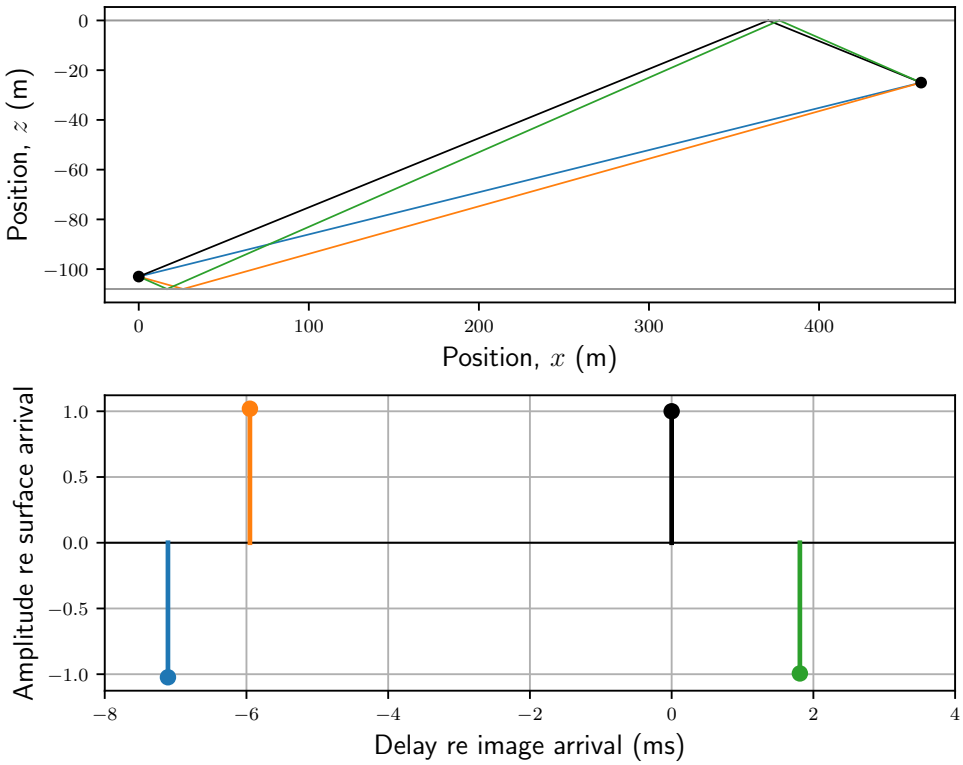

Figure 1.2: First four eigen-rays for an ideal channel: (a) eigen-rays, (b) channel impulse response. The two shortest paths in Panel (a) are the direct (blue) and bottom bounce (orange). The two surface interaction paths shown are the surface (black) and surface-bottom (green). The amplitudes of the arrivals in panel (b) have very similar magnitude, with a sign determined by the number of surface interactions. Panel (b) shows the first two paths are well separated in delay from the surface paths, which allows for the separate analysis of these two pairs of arrivals.

period of silence sets a very low upper limit to the data transmission rate. To avoid this limit, multiple symbols typically are sent within the duration of the channel impulse response and a channel equalizer system is used to recover the original sequence of symbols transmitted.[8]

When channel equalizers are used to recover the original transmission, they work best if the acoustic channel is relatively stable over multiple symbols.[17] For this reason, an important consideration in the design of a channel equalizer is the expected variation of the channel over time. This variation is quantified in at-sea experiments like KAM11 that make repeated measurements of the channel impulse response. In this data, differences between each successive measurement

of the channel impulse response can be connected to the various environmental conditions most relevant to each path. Of the channel impulse response paths, the surface paths shows the most significant variation over short periods of time and this variation is critical in the design of acoustic communication systems.[18]

1.1.2 Numerical modeling of the surface scatter

While experimental measurements are important to the understanding of acoustic scatter, numerical models often are necessary to describe or predict these results as well as to extend these results to other environments. Two commonly used models of scatter are eigen-rays and the Kirchhoff approximation.[11, 12] In addition to solving for the surface scatter, these models are useful in relating acoustic scatter arrivals to reflecting features on the surface.

Eigen-ray modeling

The eigen-ray, or geometric acoustics, solution is a high frequency approximation in which all acoustic propagation is described by rays. Acoustic rays are traced for different launch angles, and follow straight lines in the case of an iso-speed medium. When a ray encounters the surface, it reflects specularly, with equal angles of incidence and reflection. This simple calculation is the basis of the optical scatter study of Cox and Munk,[4] and is most accurate when the acoustic wavelength is shorter than the smallest physical length scale on the surface.

The eigen-ray model of the surface path is shown in Fig. 1.3 for a sinusoidal surface. Each row in Fig. 1.3 shows a different snapshot in time as the wave translates from right to left. The eigen-rays, shown in the left column of Fig. 1.3, reflect from a number of specular points on the surface. Where a flat surface predicts a single arrival (Fig. 1.2 (b)), the surface wave breaks it apart into a number of arrivals from various specular points.

The amplitude and delay of each of these eigen-rays are shown in the right column of Fig. 1.3 as an impulse response. The amplitude of each scattered arrival is generally smaller than

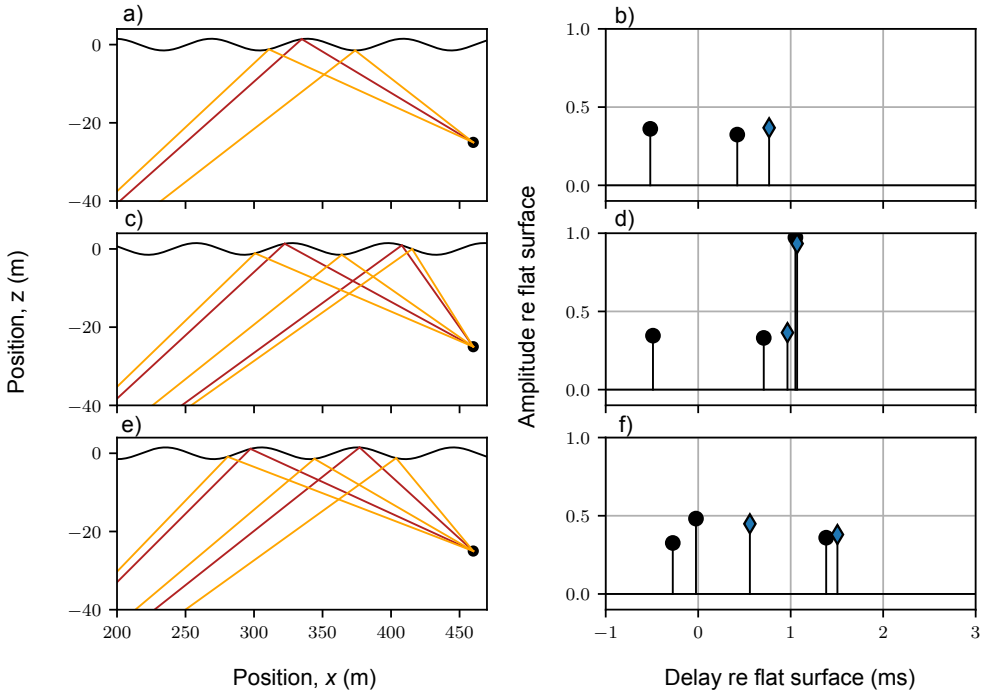

Figure 1.3: Eigen-rays and impulse response for different surface wave positions. Rays that reflect near wave troughs are shown as black circles, while rays reflecting near wave crests are shown as blue triangles.

the flat surface arrival (magnitude of 1 in these figures), although Fig. 1.3 (d) shows a focusing event at 1 ms delay with magnitude above the flat surface arrival. Additionally, the number of eigen-rays and the delay of each ray changes according to surface wave position.

While the eigen-ray solution captures much of the variability observed in surface scatter problems, the high frequency approximation used to derive eigen-rays predicts non-physical discontinuities in pressure. These discontinuous features are termed caustics and shadows zones (Ch. 3.4 in Ref. [2]). A caustic is formed at the convergence of two eigen-rays, which leads to an eigen-ray prediction of infinite amplitude. Neighboring the caustic, a shadow zone is a region where neither of the rays associated with the caustic pass, and the eigen-ray solution therefore predicts no pressure from these rays. In the eigen-ray solution, the transition region between the caustic and shadow zone is characterized by a sharp increase of amplitude up to an unbounded value at the caustic, followed by zero pressure after the caustic. The physical pressure predicted

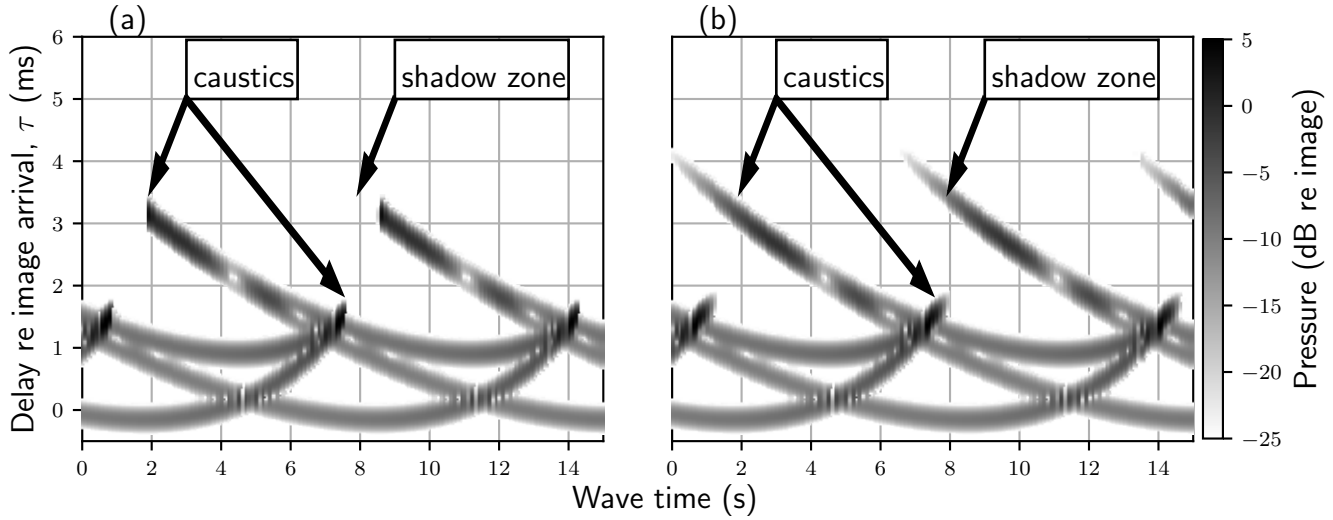

Figure 1.4: Pressure magnitude simulated with (a) eigen-rays and (b) Kirchhoff approximation. Arrows in both panels point to the same positions. The two solutions are similar up to the two discontinuous caustic features highlighted in panel (a), where the amplitude increases rapidly in the eigen-ray solution. Only one shadow zone is highlighted here, although there is a shadow zone associated with each caustic feature. In a shadow zone, no arrival is predicted by the eigen-ray solution but appears in the Kirchhoff approximation.

for this same transition instead approaches a finite value and is then followed by rapidly decaying magnitude (a similar ray-cutoff phenomena is discussed by Buckingham [19]).

Kirchhoff Approximation

While a number of different approaches have been used to address the high frequency of approximation of eigen-ray theory, the Kirchhoff approximation affords many advantages when used with surface scatter problems.[15, 12] Primarily, the Kirchhoff approximation is simple to implement and removes discontinuous features in the channel impulse response predicted by eigen-rays. Additionally, the eigen-ray result can be derived as a further approximation of the Kirchhoff approximation, which provides a consistent framework for the solution of surface scatter problems.[20]

In the Kirchhoff approximation, a ray is drawn to every position on the surface, instead of including only ray that obey specular reflection at the surface. The majority these rays are

non-physical. The Kirchhoff approximation then integrates the contribution of all of these rays, and the result of this calculation is assumed to show only physical arrivals.

The Kirchhoff approximation is compared to the eigen-ray solution in Fig. 1.4, using a physically realizable, broadband, probe signal. Unlike the theoretical impulse, the probe signal has finite duration, apparent in the vertical width of each arrival in Fig. 1.4. The eigen-ray solution in Fig. 1.4 (a) shows caustics and shadow zones at the positions indicated by arrows. The large amplitudes of the caustic are only apparent very close to the feature, but the eigen-ray solution is expected to show significant error for a range of times near the caustic. [2] The Kirchhoff approximation shown in Fig 4 (b) largely agrees well with the eigen-ray solution outside of the caustics and shadow zones. However, the Kirchhoff solution has a continuous progression of the pressure field throughout the scatter observation, a requirement of a physically consistent scatter solution.

The numerical studies of Ch. 2 and 3 work to verify the use of the Kirchhoff approximation for transmission scenarios like the ones shown in Fig. 1.1. While the Kirchhoff approximation does address the caustics and shadow zones of eigen-ray theory, it fails to completely include all scatter phenomena. There are two notable objections to the Kirchhoff approximation: (1) the treatment of surface self-shadowing and (2) multiple scatter effects. While theoretical treatments that improve the Kirchhoff approximation treat both objections solely with multiple scatter corrections,[21, 22] both issues will be discussed separately in the context of eigen-rays. First, surfaces begin to shadow themselves at longer ranges, and paths to portions of the surface require rays to leave the acoustic medium. Paths that encounter the surface more than once are typically removed from the Kirchhoff approximation, which leads to non-physical cutoffs in incident pressure along the surface.[23] Secondly, while eigen-rays may bounce two or more times along the surface before reaching the receiver, these paths are not included in the Kirchhoff approximation. The effects of these physical inconsistencies are explored by comparing the Kirchhoff approximation to an exact surface scatter solution in Ch. 2, and an improved scatter

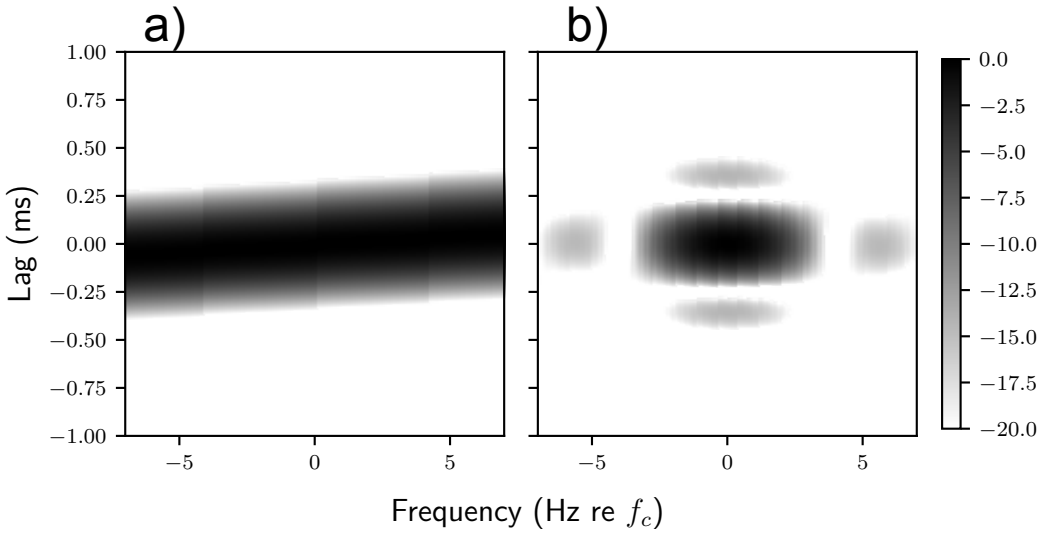

Figure 1.5: Ambiguity surface for (a) LFM and (b) MLS probe sequences. Both sequences have a center frequency of 10 kHz, and 6 kHz of bandwidth. The LFM signal is 48 ms long and the MLS signal is 256 ms long, consistent with KAM11 transmissions. Both probe signals have similar time resolution, or vertical width. The frequency, or Doppler, resolutions of both signals are significantly different. For the LFM, arrivals that are frequency shifted only produce a small change in delay time. For the MLS, arrivals that are shifted by more than 4 Hz from the matched filter template are essentially absent in impulse response estimates.

solution intended for further analysis is proposed in Ch. 3.

1.1.3 Channel probe signals and Doppler shift

Most studies of surface scatter are made using a transmission that when processed is a physically realizable approximation of the impulse. Like the numerical studies presented in Ch. 2 and 3, the scatter pressure simulations shown in Fig. 1.4 used a probe signal that was relatively short in duration. Short duration pulses are impractical, however, in experimental conditions where signal-to-noise ratio is limited. To compensate, the KAM11 transmissions used in the experiment geometry shown in Fig. 1.1 were long duration probe signals. During processing, each received transmission is cross-correlated, or match filtered, with a template of the transmitted signal for an impulse response estimate that has both short duration and large amplitude.

Two commonly used probe signals used in matched filter processing are the linear fre-

quency modulated waveform (LFM) and the maximum length sequence (MLS). These two signals are used for different applications because while they both have similar time resolution, they have different frequency resolution. The additional consideration of frequency resolution is unique to these long duration probe signals, and commonly is displayed as an ambiguity function, as in Fig. 1.5.[24] The time resolution, or vertical width of the ambiguity function, is similar for the two probe signals. The frequency resolution, or horizontal width, is significantly different.

The Doppler shift causes frequency changes in the received probe signal related to the velocity of an acoustic source or reflector. Of the two signals shown in Fig. 1.5, the LFM is relatively insensitive to Doppler (large horizontal extent) while the MLS is Doppler sensitive (narrow horizontal extent). The Doppler shift is also apparent in impulse response estimates, like those shown in Fig. 1.4, created without Doppler sensitive probe signals. A negative slope indicates an arrival decreasing in delay over time, or a positive Doppler shift. Likewise, a positive slope indicates a negative Doppler shift. The Doppler sensitive probe signals are used in Ch. 4 to emphasize these sloped arrivals in cluttered experimental measurements.

The Doppler sensitivity of the MLS is directly related to the duration of the transmitted probe signal, and longer probe signals have more Doppler sensitivity. It is common to increase the Doppler sensitivity of MLS signals by treating multiple repeats of the probe sequence as a single transmission (e.g. Preisig [17]). The changes in Doppler over time in each scattered arrival, apparent from the curved arrival shapes in Fig. 1.4, set a upper limit on the MLS template length. A single Doppler value cannot match the changing Doppler shift over the template duration, which begins to reduce the matched filter output for highly curved arrivals and long templates. For the simulation results presented in Fig. 1.5, two repeats of the 128 ms duration KAM11 MLS signal are used as a matched filter template, which give the same Doppler sensitivity as a 256 ms probe signal. A longer duration probe signal, with 640 ms duration, was chosen for the experimental data processing presented in Ch. 4 to increase the Doppler resolution of the impulse response. For the 256 ms probe signal shown in Fig. 1.5, the MLS produces almost no output

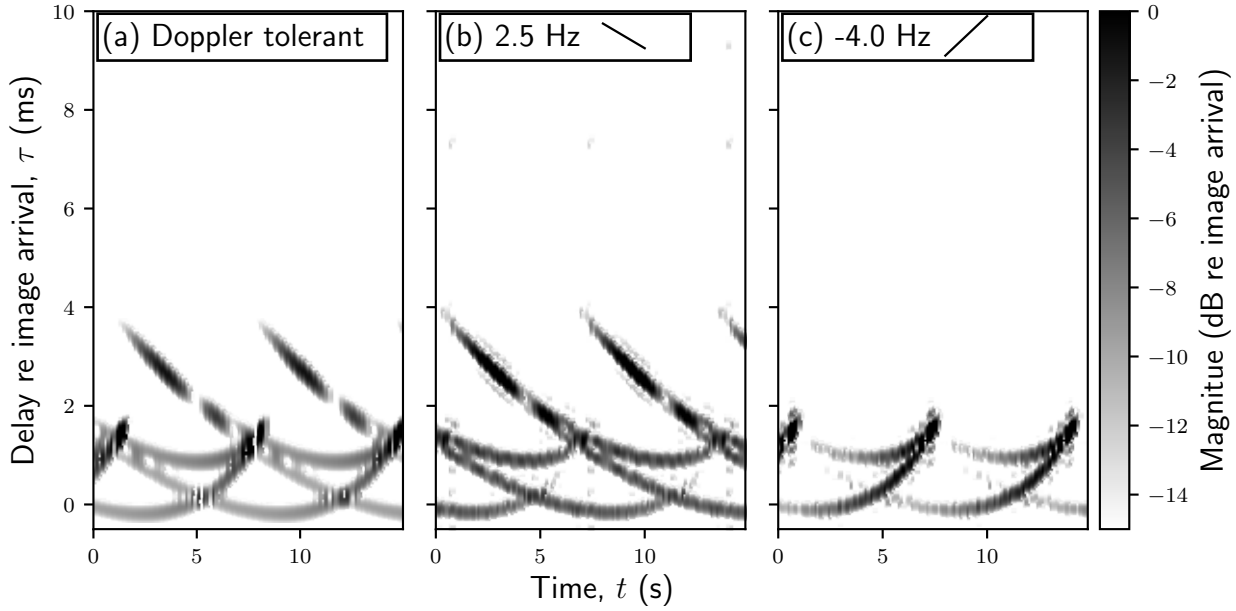

Figure 1.6: Impulse response estimate for sinusoidal surface: (a) Doppler insensitive LFM probe signal, (b) and (c) MLS probe signal with Doppler shifts of 2.5 and -4.0 Hz, respectively.

for an arrival shifted in frequency by more than 4 Hz, enabling this probe signal to distinguish arrivals with significant differences in Doppler shift.

The Doppler shift is apparent in impulse response estimates as a sloped arrival. A negative slope indicates a source decreasing in delay over time, or moving towards the observer. A positive slope indicates the opposite motion of the source. The three panels in Fig. 1.6 show channel impulse response estimates made with: (a) Doppler insensitive LFM probe signal, (b) and (c) Doppler shifted MLS templates. The Doppler shifts of the MLS templates are chosen to emphasize either the down or up slope arrivals in Fig. 1.6 (b) and (c), respectively. While the LFM is useful for presenting all scatter arrivals at once, the MLS reduces the number of arrivals apparent at a time, and removes clutter from impulse response observations. Both the LFM and MLS probe signals are used to analyze KAM11 data in Ch. 4, which also presents a more complete discussion of the observed patterns of the Doppler shift in scatter arrivals.

1.2 Summary

1.2.1 Chapter 2: Comparison of numerical scatter models

Numerical modeling is used to predict observations of scatter using a simplified model of the acoustic propagation environment. While this numerical analysis is motivated by KAM11, Ch. 2 focuses on quantifying the differences between the eigen-ray and Kirchhoff approximations and the exact scatter result. The exact, or reference, solution is computed using the Rayleigh-Fourier method (RFM). The RFM is an exact solution method limited to periodic surfaces. This study focuses exclusively on the sinusoidal surface, and uses it to show the limitations of the Kirchhoff approximation at longer ranges.

1.2.2 Chapter 3: Development of reference surface scatter model

While the numerical comparison study of Ch. 2 shows significant differences between the Kirchhoff approximation and the exact scatter result, the RFM reference solution used in this study is difficult to extend to more general sea surfaces. This led to a study of the integral equation solution for surface scatter and its solution with the limited duration integral equation method (DIEM). The DIEM is an efficient reference solution for surface scatter specifically designed for the simulation of band-limited impulse responses.

1.2.3 Chapter 4: Doppler analysis of KAM11 striation patterns

The third study presented in this thesis focuses on explaining experimental observations instead of using a numerical simulation to simulate them. The KAM11 channel impulse response estimates showed numerous late-delay arrival striation patterns that are explained as reflections from moving features on the sea surface. Doppler sensitive MLS probe signals are used to reduce significantly clutter in these measurements to clearly focus on these arrivals. The Doppler shift of

the scattered arrival and its delay then are used to estimate of the in-plane position and velocity of each surface reflector.

1.2.4 Chapter 5: Conclusions and suggestions for futher research

The numerical simulation results of Ch. 2 and 3 are intended for use in future studies that seek to improve the performance of acoustic communication systems. Furthermore, while motivated by acoustic communications, the simulation of surface scatter could inform other ocean acoustic applications, such as active sonar or acoustic tomography. The observational analysis of Ch. 4 aims to inform future research that relates physical events on the surface to changes in communication system performance. These results also suggest that a relatively focused sampling of the sea surface could significantly improve scatter modeling of experimental observations, which could be used to design future studies. Taken together, these chapters explore acoustic scatter with a variety of numerical and observational techniques, and also show some of the challenges that still remain for describing experimental results with numerical simulation.

Bibliography

[1] H. Medwin and C. Clay, *Fundamentals of Acoustical Oceanography*. Applications of Modern Acoustics, Elsevier Science, 1997.

[2] F. Jensen, W. Kuperman, M. Porter, and H. Schmidt, *Computational Ocean Acoustics*. Springer, New York, NY, 2011.

[3] W. H. Munk, R. C. Spindel, A. Baggeroer, and T. G. Birdsall, "The heard island feasibility test," *The Journal of the Acoustical Society of America*, vol. 96, no. 4, pp. 2330–2342, 1994.

[4] C. Cox and W. Munk, "Measurement of the roughness of the sea surface from photographs of the suns glitter," *Journal of the Optical Society of America*, vol. 44, no. 11, pp. 838–850, 1954.

[5] F. J. Wentz, "Measurement of oceanic wind vector using satellite microwave radiometers," *IEEE Transactions on Geoscience and Remote Sensing*, vol. 30, no. 5, pp. 960–972, 1992.

[6] G. B. Deane, J. C. Preisig, C. T. Tindle, A. Lavery, and M. D. Stokes, "Deterministic forward scatter from surface gravity waves," *The Journal of the Acoustical Society of America*, vol. 132, no. 6, pp. 3673–3686, 2012.

[7] J. C. Preisig and G. B. Deane, "Surface wave focusing and acoustic communications in the surf zone," *The Journal of the Acoustical Society of America*, vol. 116, no. 4, pp. 2067–2080, 2004.

[8] D. B. Kilfoyle and A. B. Baggeroer, "The state of the art in underwater acoustic telemetry," *IEEE Journal of oceanic engineering*, vol. 25, no. 1, pp. 4–27, 2000.

[9] M. Badiey, A. Song, and K. B. Smith, "Coherent reflection from surface gravity water waves during reciprocal acoustic transmissions," *The Journal of the Acoustical Society of America*, vol. 132, no. 4, pp. EL290–EL295, 2012.

[10] M. Badiey, J. Eickmeier, and A. Song, "Arrival-time fluctuations of coherent reflections from surface gravity water waves," *The Journal of the Acoustical Society of America*, vol. 135, no. 5, pp. EL226–EL231, 2014.

[11] Y. Choo, W. Seong, and H. Song, "Emergence of striation patterns in acoustic signals reflected from dynamic surface waves," *The Journal of the Acoustical Society of America*, vol. 136, no. 3, pp. 1046–1053, 2014.

[12] S. P. Walstead and G. B. Deane, "Reconstructing surface wave profiles from reflected acoustic pulses," *The Journal of the Acoustical Society of America*, vol. 133, no. 5, pp. 2597–2611, 2013.

[13] S. P. Walstead and G. B. Deane, "Reconstructing surface wave profiles from reflected acoustic pulses using multiple receivers," *The Journal of the Acoustical Society of America*, vol. 136, no. 2, pp. 604–613, 2014.

[14] S. P. Walstead and G. B. Deane, "Intensity statistics of very high frequency sound scattered from wind-driven waves," *The Journal of the Acoustical Society of America*, vol. 139, no. 5, pp. 2784–2796, 2016.

[15] E. I. Thorsos, "The validity of the Kirchhoff approximation for rough surface scattering using a Gaussian roughness spectrum," *The Journal of the Acoustical Society of America*, vol. 83, no. 1, pp. 78–92, 1988.

[16] M. J. Lighthill, *An Introduction to Fourier Analysis and Generalised Functions*. Cambridge Monographs on Mechanics, Cambridge University Press, 1958.

[17] J. C. Preisig, "Performance analysis of adaptive equalization for coherent acoustic communications in the time-varying ocean environment," *The Journal of the Acoustical Society of America*, vol. 118, no. 1, pp. 263–278, 2005.

[18] P. A. van Walree and R. Otnes, "Ultrawideband underwater acoustic communication channels," *IEEE Journal of Oceanic Engineering*, vol. 38, no. 4, pp. 678–688, 2013.

[19] M. J. Buckingham, "Theory of acoustic radiation in corners with homogeneous and mixed perfectly reflecting boundaries," *The Journal of the Acoustical Society of America*, vol. 86, no. 6, pp. 2273–2291, 1989.

[20] K. Williams, J. Stroud, and P. Marston, "High-frequency forward scattering from Gaussian spectrum, pressure release, corrugated surfaces. I. Catastrophe theory modeling," *The Journal of the Acoustical Society of America*, vol. 96, no. 3, pp. 1687–1702, 1994.

[21] E. Liszka and J. McCoy, "Scattering at a rough boundary – extensions of the Kirchhoff approximation," *The Journal of the Acoustical Society of America*, vol. 71, no. 5, pp. 1093–1100, 1982.

[22] D. Holliday, L. L. DeRaad, and G. J. St-Cyr, "Volterra approximation for low grazing angle shadowing on smooth ocean-like surfaces," *IEEE Transactions on Antennas and Propagation*, vol. 43, pp. 1199–1206, Nov 1995.

[23] B. Baker and E. Copson, *The Mathematical Theory of Huygens' Principle*. AMS Chelsea Publishing, American Mathematical Society, 2003.

[24] D. Eustice, C. Baylis, and R. J. Marks, "Woodward's ambiguity function: From foundations to applications," in *2015 Texas Symposium on Wireless and Microwave Circuits and Systems (WMCS)*, pp. 1–17, IEEE, 2015.

Chapter 2

Acoustic scattering comparison of Kirchhoff approximation to Rayleigh-Fourier method for sinusoidal surface waves at low grazing angles

The Fourier series method for implementing the Rayleigh hypothesis (RFM) is used as a reference solution to assess the Kirchhoff approximation of the Helmholtz integral (HKA) for modeling broadband scatter from sinusoidal surfaces at low grazing angles. The HKA is a valuable solution because it has an eigen-ray interpretation without unbounded caustic amplitudes and discontinuous shadow zones. Plane wave studies of the HKA, however, show it becomes inaccurate at low grazing angles. This study quantifies how this limitation manifests with increasing transmission distance for time domain scattering simulations. Scattering results are compared over a complete surface wave cycle with parameters modeling sea surface-swell. The HKA agrees reasonably well with RFM in point source calculations for limited extensions of transmission distances beyond where planewave comparisons begin to diverge. Past these distances, HKA solutions begin to show significant over-prediction of the acoustic amplitude around late arrivals. This over-prediction is frequency dependent and eigen-ray interference offers an explanation of this behavior. Further extending the transmission range leads to significant HKA error, and a range is found at which flat surface reflections have less error.

2.1 Introduction

Modeling time-domain acoustic scatter from deterministic, two-dimensional sea surfaces remains a computationally challenging task and practicality requires approximate methods of solution. The Helmholtz-Kirchhoff approximation (HKA) is often used for scattering calculations from general sea surfaces. It is straightforward to calculate and offers an interpretation of the solution through its eigen-ray approximation (ERA). This study seeks to establish experimental geometries where the HKA may be expected to give reasonable scattering results by comparing it to a reference Rayleigh-Fourier method (RFM). The RFM requires periodic scattering surfaces, and a sinusoidal surface is used for comparison. By establishing experimental geometries where the HKA is accurate for a simplified surface, this comparison lends credence to the approximation

for surfaces without a simple reference solution.

2.1.1 Helmholtz Kirchhoff approximation

A number of approximate surface scattering solutions exist in underwater acoustics literature, including the small slope approximation, [1] the parabolic equation, [2] the wedge assemblage method [3] and the Kirchhoff approximation of the Helmholtz integral (HKA).[4] The HKA recently has been used for wave tank studies; as a forward model in an inverse method determining the shape of the surface wave,[5] and to create scattering statistics.[6] Additionally, the HKA has been used for three-dimensional [7] and refractive environment [8] time domain scatter modeling.

The time domain form of the HKA is an extension of eigen-ray theory, building scattered time series with scaled and delayed transmissions from a number of surface interactions. The delay of each of the interactions, or rays, is the sum of the acoustic travel time to the surface point from the source and receiver. Whereas eigen-ray solutions only include contributions from rays which reflect specularly, the HKA includes rays from every point along the surface. The stationary phase approximation may be used to produce the ERA from the HKA surface integral, and each stationary point in travel time along the surface corresponding to an eigen-ray.[9]

The ERA of the HKA integral breaks down when it cannot be described with first-order stationary phase approximations. The most common breakdown of the ERA occurs in caustic regions where two eigen-rays coincide. To avoid inaccuracies introduced by the ERA this study uses numerical quadrature to solve the HKA, although higher-order stationary phase approximations provide similar results.[9] The ERA is found to be a good approximation of the HKA only short distances away from where it breaks down, however. Once the HKA result is used to find locations of interest, the ERA may be used to explain frequency-dependent focusing observed in the HKA at ranges where HKA begins to show significant error.

Describing the HKA as a superposition of rays can also explain the shortcomings of

the approximation. Planewave studies [10] have shown that the HKA becomes significantly inaccurate at lower grazing angles. This inaccuracy at low grazing angles is attributed to the inability of the HKA to model how one part of the surface interacts with the acoustic field at another part of the surface.[11] Shadowing effects, which occur when one portion of the surface blocks straight line propagation to another part of the surface, are simple to understand and test. However this study will not use shadowing corrections to the HKA because straightforward implementations did not yield any marked improvements of the results.

Meecham [4] used the Helmholtz integral equation (HIE) to study the surface self-interaction not modeled in the HKA. The HIE is a solution to the Helmholtz equation and surface boundary condition, using both the HKA and an additional integral of the unknown pressure field at the scattering surface. This unknown pressure field may be found with an iterative method that uses the HKA as an initial guess. With a stationary phase approximation of this iterative method, Liszka and McCoy [11] argued that surface shadowing is a particular multiple-scatter effect. In this solution, each iteration represents an additional surface-to-surface scattering event, either removing previous shadowed rays or adding another surface-to-surface ray to the solution. In numerical studies, however, iterative methods have shown qualified success,[12] and this makes it important to quantify the performance of the HKA before attempting to compensate for its limitations.

2.1.2 Rayleigh-Fourier Method

In addition to the iterative HIE, there exist a number of exact methods for the periodic surface scattering problem including conformal mappings,[13] direct HIE solutions using matrix inversion, and methods based on the Rayleigh hypothesis. The integral equation method is the most relevant exact solution to discussions of the HKA is because the two methods share a derivation. The direct HIE solution has been established as a reference for incident planewaves for both rough [10] and periodic surfaces.[14] However, the Rayleigh-Fourier method (RFM)

[15] was chosen over the HIE for this study because it has a straightforward implementation and efficient solution.

Scattering solution methods based on the Rayleigh hypothesis begin with a periodic surface. For planewave sources periodic surfaces give rise to Bragg scattering with a finite number of planewave propagation angles in the far-field. The periodic surface condition may be used to simplify the solution of a number of exact methods, including the HIE,[16] in terms of these Bragg scattering orders. The Rayleigh hypothesis then assumes further the boundary condition of the problem (in this case a pressure-release boundary) is satisfied on the featured surface by a superposition of out-going planewaves and an evanescent field. For the special case of sinusoidal surfaces with limited slope, the Rayleigh hypothesis has been shown to solve the boundary condition directly.[17] The slope limitations for sinusoidal surfaces are sufficient for this study on ocean surface-swell scatter, and the RFM will be considered exact in this discussion.

The RFM reference solution is also useful to determine ranges at which scattering solutions are unnecessary. In many practical experimental setups, a flat-surface reflection model may serve to explain data well. This result has been established for scattering surfaces of all types at the lower limit of grazing angles.[18] A number of different source-to-receiver ranges are used to establish when the HKA is accurate, when the image-source is accurate, and when both solutions have significant error. The range where neither solution is appropriate is found to be small, suggesting that with the appropriate choice of model, many transmission scenarios with sinusoidal surfaces can be well modeled by one of these two simple approximations.

2.1.3 Model intercomparison

The transmission scenario chosen for this study is a modest extension of wave tank studies by Walstead and Deane.[5] A high-frequency and broadband source signal was used to produce a ray-like transmission scenario for a short source-receiver x-distance, Δx, of 1.2 m (about one surface wavelength). While the surface parameters and acoustic frequencies of this numerical

study scale similarly to these studies, a number of separation distances are used to explore the limits of the HKA at low grazing angles. The first part of the model intercomparison studies fixed source and receiver geometry over a complete wave cycle, at a range where the HKA solution begins to show significant error (about five surface wavelengths).

A similar five surface wavelength geometry was also used by Choo, Seong and Song [19] to model scattering observed in channel impulse response measurements taken during sea experiments. In rapidly repeated impulse response measurements, late arriving surface scatter had coherent structure and a change in delay of about 5 ms over a few seconds of measurements.[20] This striation pattern was shown by Choo, Seong and Song [19] to arise from eigen-rays interacting with the surface close to the source or receiver. These arrivals have a longer travel distance than eigen-rays interacting with the surface near the flat surface reflection path, and result in large arrivals late in the scattered time series. This study considers a number of source-receiver separations and confirms that these eigen-rays produce a significant contribution to the scattered time series at short ranges, but find they are the largest source of error in the HKA at longer ranges.

A full description of the problem statement, and a discussion of the choice of simulation environment is covered in Sec. 2.2. The HKA, ERA, and RFM are covered in detail in Sec. 2.3. The HKA is introduced along with analytical simplifications leading to a time domain solution in Sec. 2.3.1. The further analytic approximations leading to the ERA are covered in Sec. 2.3.2. The formulation and solution method of the RFM is discussed in Sec. 2.3.3. Additionally, Sec. 2.3.3 covers the wavenumber synthesis required to create point source results. The scattered time series are computed over the full surface wave cycle at a single range in Sec. 2.4. The largest difference seen in this comparison is a frequency dependent focusing of the HKA not observed in the RFM, and this effect is explained using ERA. The maximum error between the RFM and HKA solutions is then studied for a number of ranges, and both solutions are compared with flat-surface reflection. Finally, Sec. 2.5 summarizes the study.

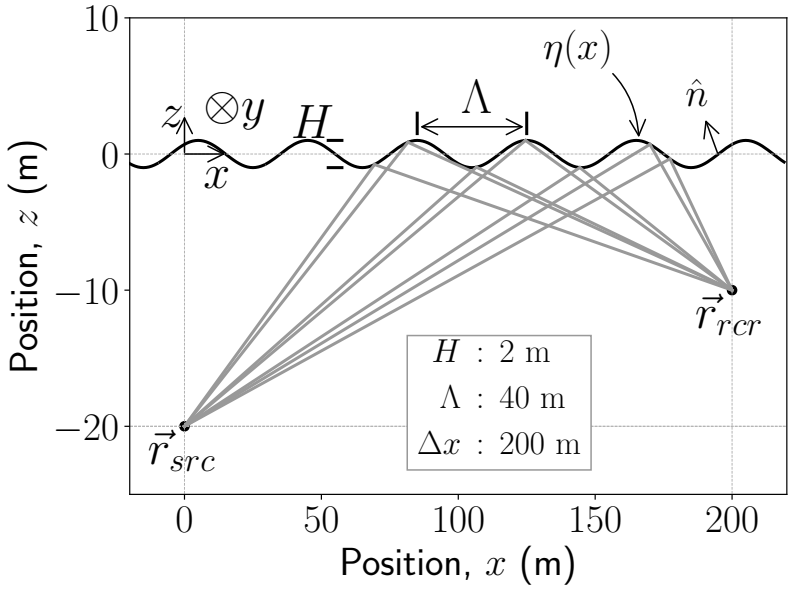

Figure 2.1: Basic schematic of the simulation setup used for Fig. 2.3, 2.6 and 2.7. The sinusoidal pressure-release surface is drawn in blue, with two characteristic length scales, height H and wavelength Λ are shown. A plane view of the surface is drawn, with the y coordinate defined as positive into the page. A radiating half space is assumed as $z \to -\infty$.

2.2 Problem statement

The three-dimensional setup of the problem along with the coordinate system is shown in Fig. 2.1. The acoustic point source is located at $\mathbf{r}_{src} = (0, 0, -10\text{m})$. The receiver is fixed at a 20-m depth, with a Δx of 200 m. For all simulations the source and receiver are separated exclusively in the x-direction, in-line with the surface wave variation.

The sinusoidal pressure-release surface is defined for wavelength Λ and wave height H as

$$\eta(x, t_{wv}) = \frac{H}{2} \cos\left(\frac{2\pi x}{\Lambda} + \phi(t_{wv})\right). \tag{2.1}$$

This study fixes the wave parameters to a 2-m wave height and 40-m wavelength. The phase of the surface wave, ϕ, is related to the surface wave time, t_{wv}, by the linear dispersion relationship. The deep-water gravity waves dispersion relationship was used in this study, $\phi(t_{wv}) = t_{wv}\sqrt{2\pi g_0/\Lambda}$, with gravitational acceleration $g_0 = 9.81\ m/s^2$.

The time variation of the surface wave is solved as a succession of frozen surfaces, assuming that the movement of the ocean surface is much slower than the sound speed in water. Similar to the argument in Walstead and Deane,[5] the short time duration of the transmitted pulse makes it insensitive to the motion of the sea surface. While a full time domain solution is required to quantify this approximation, eigen-rays are used to justify the frozen surface assumption based on two arguments. First, all eigen-rays interact with the surface within a millisecond of each other, and so all relevant acoustic paths encounter essentially the same wave shape. Secondly no significant Doppler shift is expected, since for the duration of the acoustic pulse the motion of the surface is a small fraction of the shortest acoustic wavelength.

For a frozen surface and an acoustic time dependence of $\exp(-i2\pi ft)$, the acoustic pressure, $P(x,y,z)$, satisfies the Helmholtz equation

$$(\nabla^2 + k^2)P(x,y,z) = 0. \tag{2.2}$$

Upper case letters indicate frequency domain functions. The acoustic wavenumber, k, is defined in terms of the acoustic frequency, f, through the dispersion relationship, $k = 2\pi f/c$. The sound speed in the medium, c, is fixed at 1500 m/s.

The total pressure field is split into a sum of two fields, $P(x,y,z) = P_{inc}(x,y,z) + P_{sc}(x,y,z)$. $P_{inc}(x,y,z)$, is the known incident pressure field of an acoustic source in a homogeneous, unbounded medium. $P_{sc}(x,y,z)$, is the unknown scattered pressure field determined by the boundary conditions. The pressure-release boundary condition is

$$-P_{inc}(x,y,\eta(x)) = P_{sc}(x,y,\eta(x)). \tag{2.3}$$

A radiating boundary condition is required to fully define the problem and can be expressed in general terms.[21] For incident planewaves, the general radiating condition of the scattered pressure for a homogeneous and otherwise unbounded medium is simplified to an outgoing

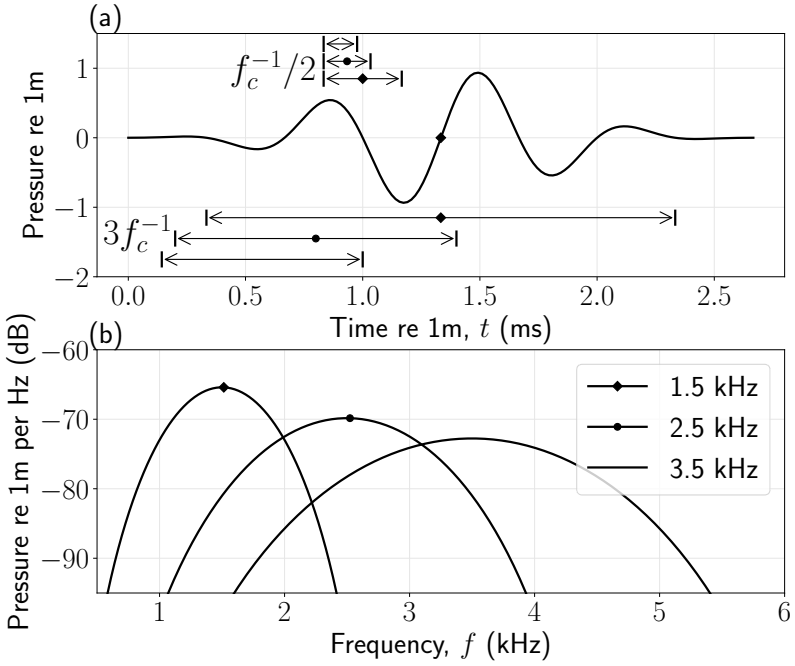

Figure 2.2: (a) Time series of 1.5 kHz center frequency transmission, $s(t)$. (b) Fourier transforms of all three transmitted signals, $S(f)$, showing the signals bandwidth are roughly equal to the carrier frequencies: 1.5 , 2.5 and 3.5 kHz. All three of the transmitted time series are constructed as four-cycle sinusoids, windowed with a Kaiser-Bessel function, and have the same shape in the time domain. The scaling of the center frequency of the sinusoid has the effect of changing the time scales of the signal, including the half cycle period, $f_c^{-1}/2$, and the duration, defined as $3\ f_c^{-1}$.

wave condition.[15] The outgoing wave condition specifies that, for an incident planewave, the scattered pressure field below the minimum extent of the surface consists only of planewaves propagating in the $-z$ direction and an exponentially decaying evanescent field.

As shown in Fig. 2.2, simulation test signals, $s(t)$, are four-cycle sinusoids at three center frequencies: 1.5, 2.5 and 3.5 kHz. A Kaiser-Bessel window with design parameter 2.5 π (α in [22]) is applied to reduce side lobes in the frequency domain representation of the signal, $S(f)$. The scattered time series is the real part of the analytic signal given by the one-sided Fourier transform of the signal spectra, $S(f)$, and the pressure field, $P_{sc}(x,y,z,f)$,

$$p_{sc}(x,y,z,t) = 2\,\mathrm{Re}\left\{ \int_0^\infty P_{sc}(x,y,z,f) S(f) \exp(-i2\pi f t) df \right\}. \tag{2.4}$$

Note that the sign convention adopted here, where positive k values give waves outgoing with time, is opposite to that of the discrete Fourier transform.

2.3 Scattering solution methods

The comparison of HKA and RFM solutions in this study are primarily between scattered time series from acoustic point sources. However, the RFM solution exists only for planewave sources, and both wavenumber and frequency syntheses are required to produce these time series. In contrast, the HKA has a simple integral form for point sources,[9] in addition to a closed-form solution for planewaves.[23] The time domain form of the HKA is derived in 2.3.1. The RFM and the additional wavenumber integration required to produce point source results are covered in Sec 2.3.3.

2.3.1 Helmholtz Kirchhoff approximation

The HKA is an expression for the total pressure field along a boundary in terms of the incident pressure field. This approximation, also known as the local tangent approximation, is equivalent to constructing the scattered field from an integral of infinitesimal flat surface reflections. For a pressure-release boundary, the HKA is

$$\frac{\partial P}{\partial n}(\bar{\mathbf{r}}) \approx 2\frac{\partial P_{inc}}{\partial n}(\bar{\mathbf{r}}). \tag{2.5}$$

An over-bar is used to indicate a position vector along the surface and for each value of (x,y), the z value of the vector $\bar{\mathbf{r}}$ is $\eta(x,y)$. A vector along the surface may be defined alternatively as points at which the function $g(\bar{\mathbf{r}}) = 0$, convenient for surface normal and projected surface area

calculations. The definition of $g(x,y,z)$ consistent with the outward surface normal direction, $\hat{n}$, (shown in Fig. 2.1) is $g(x,y,z) = z - \eta(x,y)$.

The incident field, P_{inc}, is determined using the free-space Green's function. For iso-speed media,

$$G(\mathbf{r}_{src}, \mathbf{r}_{rcr}) = \frac{\exp(ikd_{sr})}{4\pi d_{sr}}, \quad \nabla G(\mathbf{r}_{src}, \mathbf{r}_{rcr}) \approx ik \frac{(\mathbf{r}_{rcr} - \mathbf{r}_{src})}{d_{sr}} \frac{\exp(ikd_{sr})}{4\pi d_{sr}}, \tag{2.6}$$

where $\mathbf{r}_{src}$ and $\mathbf{r}_{rcr}$ are vectors of source location and observation point, respectively, and $d_{sr} = |\mathbf{r}_{rcr} - \mathbf{r}_{src}|$. The far-field approximation was used to simplify the Green's function gradient. The incident normal derivative term of Eq. (2.5), $\partial P_{inc}(\bar{\mathbf{r}})/\partial n$, is calculated from Eq. (2.6) using the operator $\partial/\partial n = \hat{n} \cdot \nabla$.

Green's theorem relates the scattered pressure at the receiver to the pressure field at the surface. Excluding the source from the integration volume following Holford,[24] Green's theorem [21] along the pressure-release surface and the radiating boundary is

$$P_{sc}(\mathbf{r}_{rcr}) = \frac{1}{4\pi} \iint_{-\infty}^{\infty} \frac{\exp\left(ik|\mathbf{r}_{rcr} - \bar{\mathbf{r}}|\right)}{|\mathbf{r}_{rcr} - \bar{\mathbf{r}}|} \Psi(\bar{\mathbf{r}}) dx\, dy, \tag{2.7}$$

where the vector $\bar{\mathbf{r}}$ depends on (x,y). The function, $\Psi(\bar{\mathbf{r}})$, is introduced as the product of the normal derivative of the pressure field with the surface differential scaling term, $\Psi(\bar{\mathbf{r}}) = |\nabla g(x,y,\eta)|\, \partial P(x,y,\eta)/\partial n$, projecting the integral onto the $z = 0$ plane.

The HKA is expressed as a two-dimensional integral using the approximation of (2.5) in Eq. (2.7). The resulting integral can be evaluated using numerical quadrature or approximate methods such as stationary phase.[25] Either method can be applied to one or both of the integrals. For the flat surface, two applications of the stationary phase approximation to the HKA integral give the exact image-source solution, $-\exp(ikd_{img})\ (4\pi d_{img})^{-1}$, where d_{img} is the image-source distance.

Following Walstead and Deane,[5] the stationary phase approximation is applied along the y-axis to reduce the surface integral dimension to one. This approximation produces exact

results for the surface under study since the y-dimension is an infinite line for each value of x,

$$P_{sc}(\mathbf{r}_r) = \exp(i\,3\pi/4)\,\sqrt{\frac{k}{2\pi}}\int_{-\infty}^{\infty}\frac{(\bar{\mathbf{r}}-\mathbf{r}_{src})\cdot\nabla g}{d_{src}}\frac{\exp\left[ik(d_{rcr}+d_{src})\right]}{\sqrt{(d_{rcr}+d_{src})d_{rcr}d_{src}}}dx. \tag{2.8}$$

The scalar distances d_{src} and d_{rcr} are $|\bar{\mathbf{r}}-\mathbf{r}_{src}|$ and $|\mathbf{r}_{rcr}-\bar{\mathbf{r}}|$, respectively.

The form of Eq. (2.8) allows for analytical evaluation of the Fourier synthesis, Eq. (2.4), resulting in a time domain equation. With one exception, each of the terms of Eq. (2.8) depend either on the spatial variable, x, or on the wavenumber, k. After changing the order of spatial and frequency integration, the terms depending on x can be brought outside the Fourier synthesis integration. The only function that has both spatial and wavenumber variables is $\exp[ik(r_{src}+r_{rcr})]$, representing the time shift $\tau(x) = (r_{src}+r_{rcr})/c$. Collecting all complex and frequency dependent terms into the inverse Fourier transform gives the filtered and delayed signal function,

$$s_{hk}(t-\tau) = \mathcal{F}^{-1}\left(\exp(i\,3\pi/4)\sqrt{f}\,S(f)\exp(i\,2\pi f\,\tau)\right). \tag{2.9}$$

The time domain HKA is then

$$p_{sc}(\mathbf{r}_{rcr},t) = \sqrt{\frac{1}{c}}\int_{-\infty}^{\infty}\frac{(\bar{\mathbf{r}}-\mathbf{r}_{src})\cdot\nabla g(x,z)}{d_{src}}\frac{s_{hk}(t-\tau(x))}{\sqrt{(d_{rcr}+d_{src})d_{rcr}d_{src}}}dx. \tag{2.10}$$

2.3.2 Eigen-ray approximation to the Kirchhoff approximation

The HKA scattering solution can be reduced from an integral to a sum of discrete scattering points using the stationary phase approximation for all integrals in equation (2.7). Barring multiple bounce reflection paths and surface shadowing, the result is equivalent to geometrical acoustics.[9] Geometric acoustics is a high frequency limit, and expected to give better results with increasing source frequencies. Each term in the stationary phase sum is termed an eigen-ray, and is characterized by a complex amplitude and delay. This approximation then

solves for the scattered pressure field as an interference of a few arrivals from different parts of the scattering surface.

The stationary phase approximation is applied to equation (2.8). Collect all non-exponential terms of this equation into the slowly varying function $A(x)$,

$$P_{sc}(\mathbf{r}_r) = \exp(i3\pi/4)\,\sqrt{\frac{f}{c}}\int_{-\infty}^{\infty} A(x)\exp\left[i\,2\pi f\tau(x))\right]dx. \tag{2.11}$$

This leads to the approximate scattering solution

$$P_{sc}(\mathbf{r}_r) = \frac{\exp\left(i\left[3\pi/4 \pm \pi/4\right]\right)}{\sqrt{c}}\sum_n \frac{A(x_n)}{\sqrt{|\tau''(x_n)|}}\exp\left(i\,2\pi f\tau(x_n)\right). \tag{2.12}$$

The prime notation, $'$, is used to denote a derivative with respect to x. The sum in Eq. (2.12) is carried over the n points at which $\tau'(x_n) = 0$. The sign inside the exponential of Eq. (2.12) is the same as that of $\tau''(x_n)$.

As with the HKA, the Fourier synthesis of the ERA can be evaluated analytically. Two different signals are used in the scattered solution, dependent on the sign of $\tau''(x_n)$. Positive $\tau''(x_n)$ gives a real amplitude term which contributes a delayed and scaled version of the transmitted signal to the scattered result. Negative $\tau''(x_n)$ gives an imaginary amplitude term and contributes a phase shifted version of the transmitted signal,

$$s_-(t-\tau) = -\mathcal{F}^{-1}\left(i\,S(f)\exp(i\,2\pi f\,\tau)\right). \tag{2.13}$$

A negative sign is included for consistency in later notation, and this result is the Hilbert transform by standard convention.[26]

Denoting the unmodified transmitted signal as s_+, the scattered pressure field in the time

domain is expressed

$$P_{sc}(\mathbf{r}_r) = -\frac{1}{\sqrt{c}} \sum_n \frac{A(x_n)}{\sqrt{|\tau''(x_n)|}} s_{\pm}(t - \tau(x_n)). \tag{2.14}$$

Again, the sign choice for the signal interpolator, $s_{\pm}(t)$, is the same as that of $\tau''(x_n)$. This sum represents the sum of two convolutions, one for $s_{-}(t)$ and $s_{+}(t)$, with a channel represented as a few scaled delta functions.

The ray travel time, $\tau(x)$, and its derivatives are important to determining the amplitude, position and delay of each eigen-ray. In Fig. 2.3(b), the total travel time is plotted for the example of the surface wave at $t_{wv} = 0.70$ s. The overall bowl-like shape of $\tau(x)$ is similar to that of the flat surface reflection, with deviations in travel time related to the surface profile. Stationary points appear or disappear from this curve in pairs, preserving the direction of the derivatives at the edges of this curve. The appearance of a pair of stationary points on $\tau(x)$ occurs in three steps: 1) the travel time curve near an edge flattens, 2) two stationary points coincide on the curve, 3) points are separated in space. The first two steps create eigen-ray shadow and caustic regions, respectively. In eigen-ray shadow regions the stationary phase approximation does not include contributions from a significant region. In eigen-ray caustic regions, $\tau''(x)$ approaches 0 and Eq. (2.14) grows unbounded.

The interference pattern between multiple eigen-rays means that different source signals have different behaviors for the same channel. For the signal used in this simulation the interference for two rays is largely determined by center frequency of the signal, f_c, and the spacing of rays less than one period apart, f_c^{-1}. When two signals have the same sign of $\tau''(x_n)$ maximum constructive interference occurs with no delay and maximum destructive interference occurs at half period delay, $f_c^{-1}/2$. For a ray pair, the difference in $\tau''(x_c)$ sign means maximum constructive interference occurs at quarter period delay, $f_c^{-1}/4$, and maximum destructive interference at three quarter period delay, $3f_c^{-1}/4$. Away from eigen-ray shadow and caustic regions, the interferences predicted by the ERA agree well with the HKA and explain large peak amplitudes observed in the HKA.

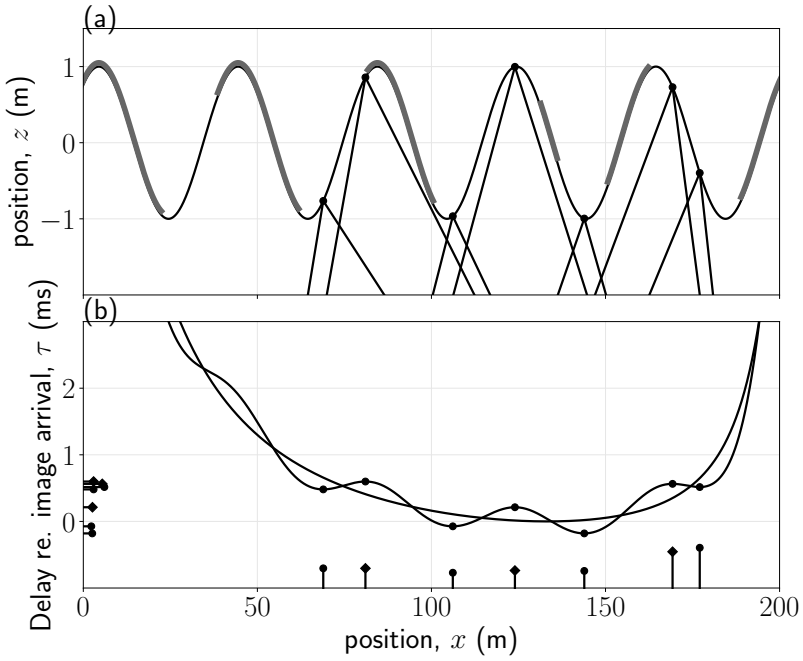

Figure 2.3: Simulation setup of Fig. 2.1, wave at t_{wv}=0.70 s. (a) Spatial position of surface with eigen-rays. Eigen-rays connect the source and receiver and obey specular reflection at the surface (differences in spatial scales may distort perceived angles). Thick patches are shadowed areas of the wave where rays intersect the surface more than once. (b) Travel time, $\tau(x)$, for ray connecting the source and receiver at each point on the surface. Travel time curve for flat surface is the smooth light line. Relative eigen ray amplitudes are shown as a function of both position and delay. Rays with circles have real amplitude, while rays with diamonds have imaginary amplitude. The ray pair closest to the receiver have the largest ray amplitudes, which contribute to a cluster of rays near 0.6 ms delay.

The travel time curve for the wave position of Fig. 2.1 is shown in Fig. 2.3. The paths of each eigen-ray, which connect the source and receiver through a specular reflection, are drawn in Fig. 2.3(a). Each of the extrema of $\tau(x)$ in Fig. 2.3(b) corresponds to an eigen-ray in Fig. 2.3(a). In the center of the wave profile eigen-rays appear at the peaks and troughs, while closest to the source and receiver the ray pairs appear on the same wave face. The largest eigen-rays occur in a pair on the wave face closest to the receiver, and these share a delay similar to that of the smaller eigen-ray pair closest to the source. These late arrival features are found consistent in the HKA and ERA solutions for a number of source-receiver x-separations, section 2.4.2.

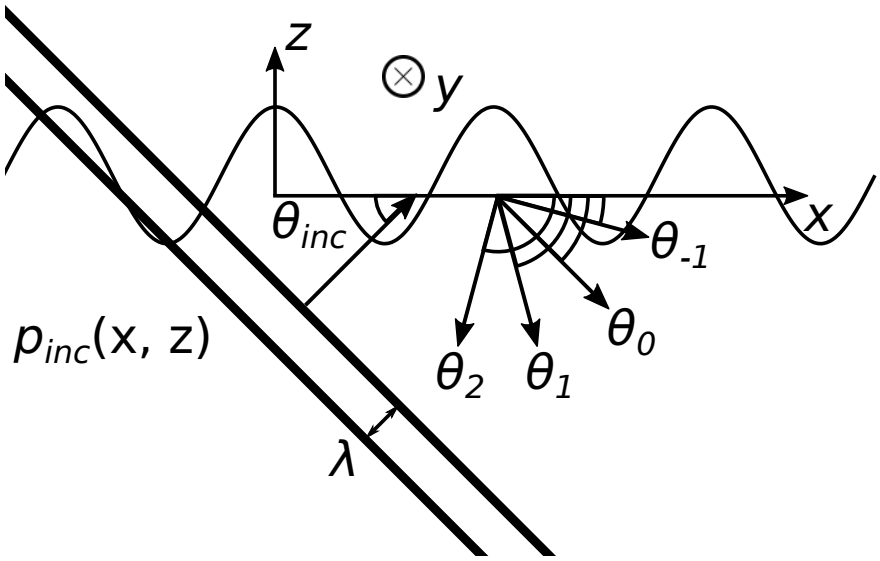

Figure 2.4: Schematic of the Rayleigh expansion. An incident planewave propagates with angle θ_{inc} towards the pressure-release surface. Two lines of constant phase are shown with a one acoustic wavelength, λ, spacing. The incident field does not interact with the surface, and the constant phase lines are drawn through the surface as though it were not there. The Bragg scattering angles are numbered, where θ_0 is the specular reflection angle when $\cos(\theta_{inc}) = \cos(\theta_0)$.

2.3.3 Rayleigh expansion and hypothesis

For an incident planewave on a periodic surface, the expansion of the scattering solution into a discrete sum of plane and evanescent waves is known as the Rayleigh expansion, represented schematically in Fig. 2.4. The expansion is the result of the surface periodicity and the planewave radiation condition. The unknown scattered field is also expressed as the product of an unknown function periodic with scale Λ, and the function $\exp(i\alpha_{inc}\, x)$,[15]

$$P_{sc}(x,z) = \exp(i\alpha_{inc}\, x) \sum_{n=\infty}^{\infty} R_n Z(z) \exp\left(\frac{i2\pi n x}{\Lambda}\right), \tag{2.15}$$

where the unknowns R_n are the sound pressure *reflection coefficients*. The unknown function, $Z(z,n)$, is determined by Eq. (2.2) and the OWC,

$$Z(z,n) = \exp(-i\gamma_n z), \quad \gamma_n = \sqrt{k^2 - \left(\alpha_{inc} + \frac{2\pi n}{\Lambda}\right)^2}. \tag{2.16}$$

The Rayleigh hypothesis then makes the assumption that the Rayleigh expansion converges to the true pressure field at the pressure-release surface itself.[27] This hypothesis holds for sinusoidal scattering surfaces with maximum slope ($\pi H/\Lambda$) of 0.448 or less,[17] but not for general periodic surfaces. When this hypothesis holds, the scattering problem is simplified to finding the complex amplitudes of an number of outgoing planewaves. This study uses the Rayleigh-Fourier method (RFM) to solve for these unknown amplitudes, leading to an infinite system of equations relating Fourier series coefficients. The Galerkin method is used to solve this infinite system of equations, simply truncating it after a few evanescent orders. The reflection coefficients from this method conserved energy beyond 99.9% [24] for all calculated values, and are considered exact.

Each term in Eq. (2.15) represents a plane or evanescent wave with horizontal wavenumber $\alpha_n = \alpha_{inc} + 2\pi n/\Lambda$, and vertical wavenumber, γ_n. The propagation direction of these planewave are the Bragg angles,[15]

$$cos(\theta_n) = \cos(\theta_{inc}) + n\frac{\lambda}{\Lambda}. \tag{2.17}$$

Each term with $|\cos(\theta_{inc}) + n\lambda/\Lambda| < 1$ is a planewave propagating away from the surface, and otherwise is an evanescent wave decaying exponentially as $z \to -\infty$.

The RFM uses the expansion of Eq. (2.15) directly in the boundary condition of Eq. (2.3). The resulting equality between two periodic functions is solved as an equality between Fourier coefficients. For the sinusoidal surface of Eq. (2.1), the Fourier coefficients are analytic, and the

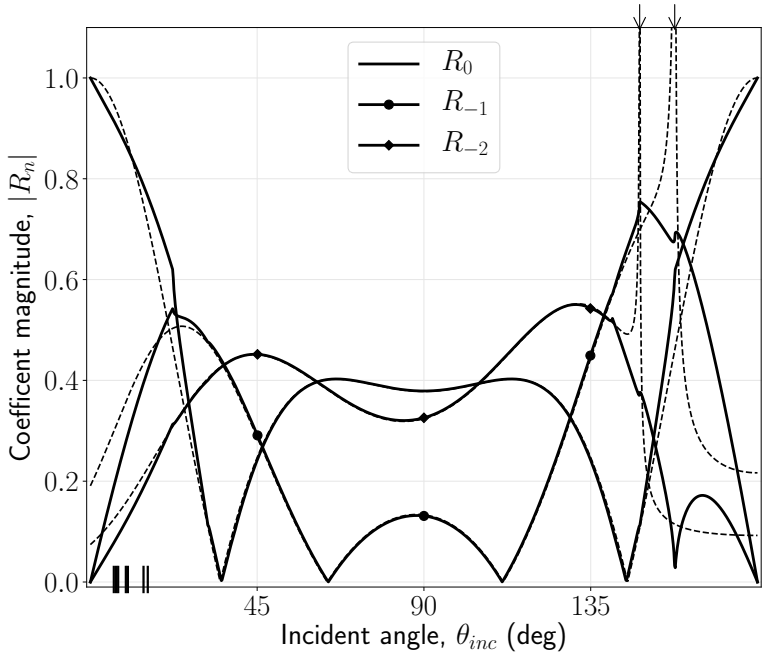

Figure 2.5: Magnitude of the reflection coefficients, $R_n(\alpha_{inc})$, computed using RFM and HKA at 500 Hz for a sinusoidal surface with a 2-m wave height and a 40-m wavelength. The RFM results are plotted as solid lines, while the HKA is plotted as lighter dashed lines. For symmetric surface profiles, the reflection coefficients of order n are the same as that for order $-n$, mirrored about $\theta_{inc} = 90°$. The angles at which each Bragg order becomes evanescent are marked on top of graph with arrows, and the HKA coefficients grow unbounded at these angles. The incident angles of the eigen-rays for the experimental setup of Fig. 2.1 at t_{wv}=0.70 s are plotted as ticks along the bottom axis.

RFM gives

$$-i^m J_m\left(\gamma_{inc}\frac{H}{2}\right) = \sum_{n=-\infty}^{\infty} i^{n-m} R_n J_{n-m}\left(-\gamma_n\frac{H}{2}\right), \tag{2.18}$$

where J_m is a Bessel function of the first kind with order m. This infinite system of equations is solved by truncation after a finite number of terms. Three positive and three negative evanescent orders of n were found sufficient for energy conservation, while including too large a number of evanescent orders introduced numerical instability.

For comparison with RFM calculations, the reflection coefficients of the HKA have a

closed form,[23]

$$R_n = i^n \, \frac{\alpha_{inc}(\alpha_n - \alpha_{inc}) - \gamma_{inc}(\gamma_{inc} + \gamma_n)}{\gamma_n(\gamma_{inc} + \gamma_n)} \, J_n\big((\gamma_{inc} + \gamma_n)H/2\big). \tag{2.19}$$

The phase term, i^n, was added to this expression following McCammon and McDaniel,[28] and gives $R_0 = -1$ when $H = 0$.

The HKA and RFM reflection coefficients are shown at 500 Hz in Fig. 2.5. This low frequency was chosen for ease of visualization because it has the least variation with θ_{inc}, but the behavior comparison is similar at higher frequencies. The surface profile is symmetric about $x = 0$, requiring $R_n(\theta_{inc}) = R_{-n}(180^\circ - \theta_{inc})$. The HKA coefficients are indistinguishable from the RFM for θ_{inc} between 40° and 140°, covering near-vertical incidence. All of the eigen-rays angles for the test scenario of Fig. 2.1 are less than 20°, and are indicated as copper ticks along the θ_{inc} axis in Fig. 2.5. For negative Bragg orders, these angles are past where the two solution methods diverge, below $\theta_{inc} = 40^\circ$. The largest discrepancy between the RFM and the HKA solutions is largest at the cutoff angle for each Bragg order (31.7° and 22.3° for orders 2 and 1), where the HKA predicts unbounded amplitude, while the RFM remains bounded.

A wavenumber synthesis is required to produce point source scattering from the planewave results of the RFM,

$$P_{sc}(\mathbf{r}) = \frac{i}{8\pi^2} \sum_{n=-\infty}^{\infty} \iint_{-\infty}^{\infty} R_n(\alpha_{inc}, \beta) \frac{\exp\left(i \left[\begin{bmatrix} \alpha_n \\ \beta \\ -\gamma_n \end{bmatrix} \cdot \mathbf{r}_{rcr} - \begin{bmatrix} \alpha_{inc} \\ \beta \\ \gamma_{inc} \end{bmatrix} \cdot \mathbf{r}_{src} \right] \right)}{\gamma_{inc}} d\alpha_{inc} \, d\beta. \tag{2.20}$$

The horizontal wavenumber in the y-dimension is introduced as β, with the requirement $k^2 = \alpha^2 + \beta^2 + \gamma^2$. Holford [24] noted that for y-independent surfaces, the solution for $R_n(\alpha_{inc}, \beta)$ at all β can be constructed from the planewave with $\beta = 0$ and a modified value of $k_{2d}^2 = k^2 - \beta^2$.

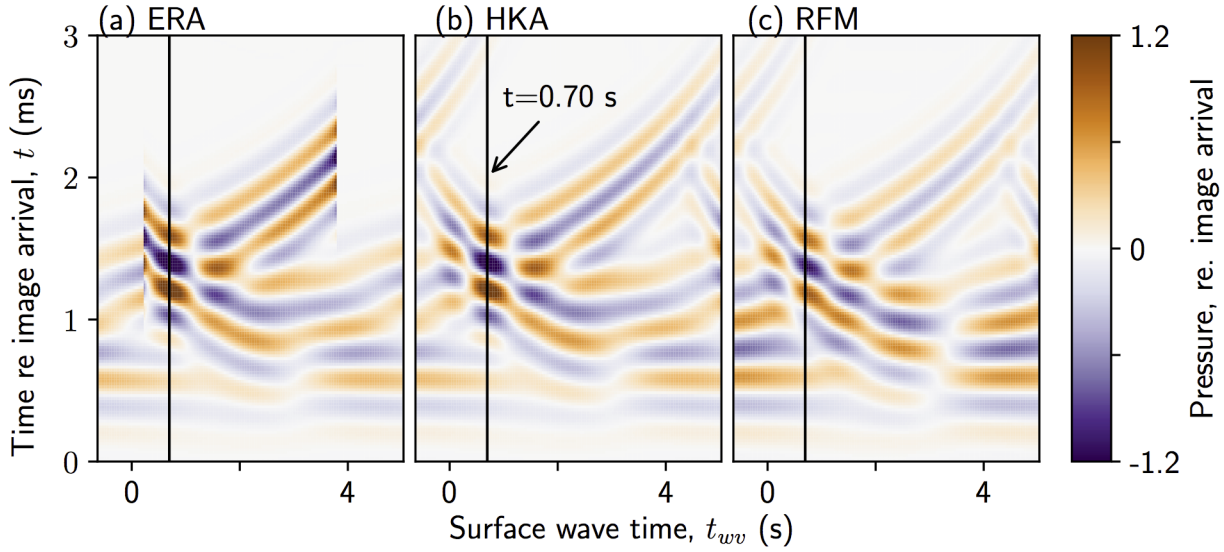

Figure 2.6: Scattered time series plotted over a single surface wave period for 2.5 kHz center frequency pulse and simulation setup of Fig. 2.1: (a) ERA, (b) HKA, and (c) RFM results. The scattered pressure, $p_{sc}(t)$, is plotted referenced to the image (flat surface) arrival.

The stationary phase approximation in α_{inc} and β is used to compute point source results from Eq. (2.20). The phase function of the wavenumber integral is simple, with a single stationary point for each term in Eq. (2.20). For source and receivers at $y = 0$, the stationary phase approximation is

$$P_{sc}(\mathbf{r}) \approx \sum_{n=-\infty}^{\infty} R(\alpha_{inc}) \frac{\exp\left[i(\alpha_n x_r - \alpha_{inc} x_s - \gamma_n z_r + \gamma_{inc} z_s)\right]}{4\pi k \gamma_{inc}} \left(\left| \frac{z_r}{\gamma_{inc}^3} + \frac{z_s}{\gamma_n^3} \right| \left| \frac{z_r}{\gamma_{inc}} + \frac{z_s}{\gamma_n} \right| \right)^{-1/2}. \tag{2.21}$$

This function is evaluated at stationary points when $x_s = x_r + \alpha_n z_r/\gamma_n + \alpha_{inc} z_s/\gamma_{inc}$. The errors associated with the stationary phase approximation are related to the rapidly changing values of $R_n(\alpha_{inc})$, evident in Fig. 2.5. These errors were found to be small by comparing synthesized HKA results using Eqs. (2.19) and (2.21) with time series solutions computed using Eq. (2.10).

2.4 Results

Time series transmissions are compared between the HKA of Eq. (2.10), the ERA of Eq. (2.14), and the RFM constructed with the wavenumber and time synthesis of Eqs. (2.21) and (2.4). To highlight the effect of the featured surface, the amplitudes in the following plots are divided by the amplitude of the image arrival, $(4\pi r_{img})^{-1}$, and the image delay, r_{img}/c, is subtracted from the acoustic time scale, t. For the first part of the results discussion Δx is fixed at 200 m. The surface wave position is allowed to vary as a function of wave time, t_{wv}, according to Eq. (2.1). For the second part of the discussion, Δx is varied between 50 and 1000 m. A single wave position is chosen for each range which produces the largest peak arrival in the HKA results. The remaining simulation parameters are constant, as discussed in Sec. 2.2 and plotted in Fig. 2.1.

2.4.1 Full surface wave cycle simulations

The 2.5 kHz signal scattered time series is presented as color-maps in Fig. 2.6 over the full surface wave cycle for $\Delta x = 200$ m. There is good agreement between the HKA and RFM in the time dilation of the pulse, the distribution of energy through the scattered arrival, and the location of major focusing events. The ERA and the HKA are in agreement up until the caustic region, apparent in the ERA as a sharp increase in amplitude followed by sudden disappearance of acoustic pressure. In contrast, the HKA predicts a smooth decrease of acoustic pressure through this region.

The largest discrepancy between HKA and RFM is in the amplitudes of the largest peak pressure, around surface wave time, t_{wv}, of 0.70 s (indicated by vertical line in Fig. 2.6). These scattering results are shown in Fig. 2.7 for three acoustic center frequencies: (a) 3.5, (b) 2.5, and (c) 1.5 kHz. There are no significant eigen-ray shadow or caustic regions near the receiver, and ERA does well predicting the HKA result. For the higher source frequencies shown in Fig.

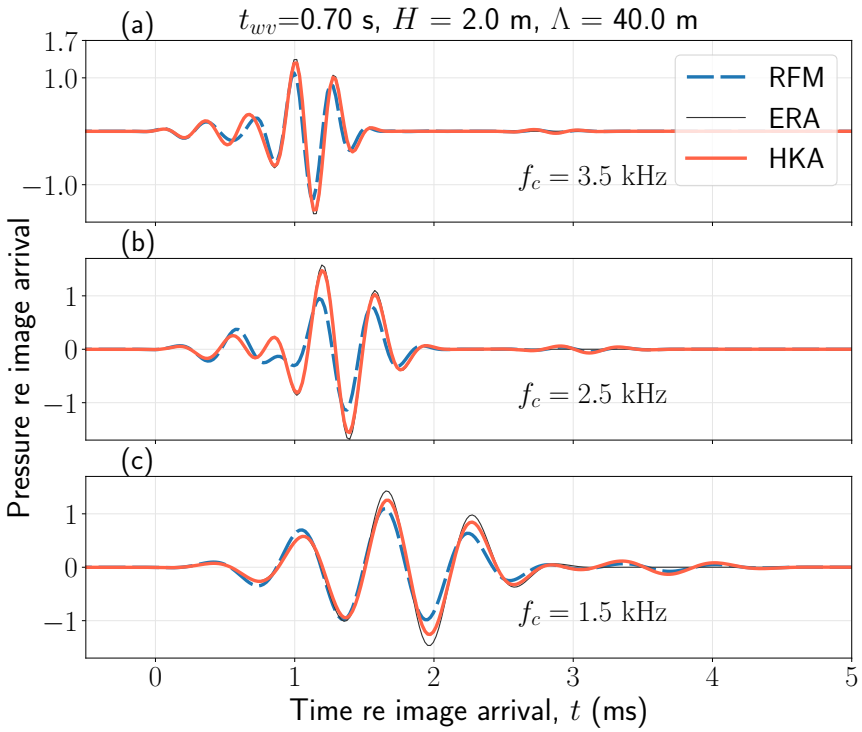

Figure 2.7: Scattered time series for surface wave phase at $t_{wv} = 0.70$ s, using the simulation setup shown in Fig. 2.1. Each panel shows results for one of three source center frequencies, f_c, computed using RFM, the HKA and the ERA: (a) 3.5, (b) 2.5, and (c) 1.5 kHz. The shape of the time series is similar between the RFM and HKA solution methods, though the HKA consistently over-predicts the largest amplitudes at each center frequency. The HKA over-prediction is greatest for the 2.5-kHz transmission between 1 ms and 1.5 ms. The ERA agrees well with the HKA, with a slight overprediction, largest at 1.5 kHz.

2.7(a) and 2.7(b), the rays that make up the scattered time series are separated in time, with low amplitude arrivals before 1 ms, and higher amplitude arrivals after 1 ms delay. This structure is not apparent in Fig. 2.7(c), where the longer time width of the 1.5 kHz signal merges the eigen-ray arrivals. For all frequencies, this surface wave position leads to focusing and the late arrival amplitudes exceed the image arrival (*i.e.* > 1).

While the HKA over-estimates the signal amplitude for almost the entire time series for each frequency, the most significant disagreement between the solutions is for the peak pressures at the middle probe signal frequency (2.5 kHz; Fig. 2.7(b) around 1.5 ms). The eigen-ray arrival structure for 200-m Δx, shown in Fig. 2.8(a), produces an ERA result is similar to the HKA.

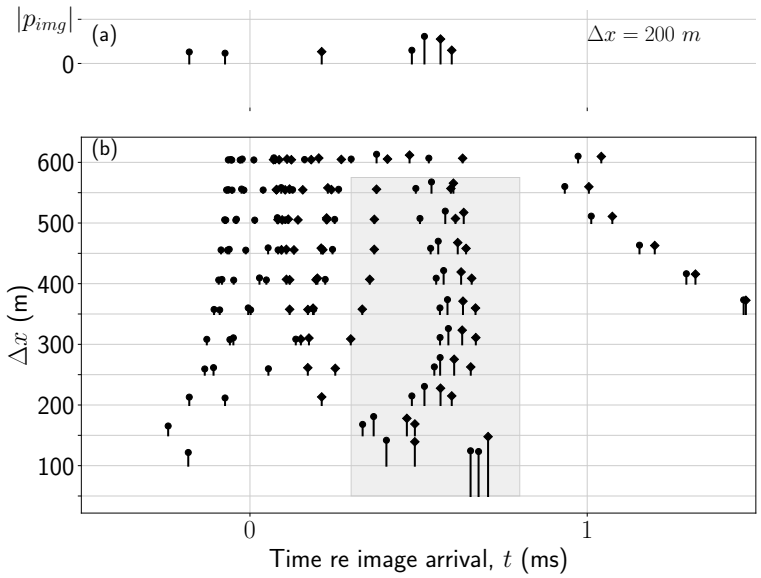

Figure 2.8: Eigen-ray delay and amplitude, normalized to image arrival, for the wave position creating the largest HKA peak amplitude. Rays with circles have real amplitude, while rays with diamonds have imaginary amplitude. Panel (a) are the rays for the test setup of Fig. 2.1. Panel (b) shows rays making up the largest HKA peak arrival at 50-m increments of source-receiver separation. The approximate delay times of the largest arrivals are highlighted in grey for ranges with strong late arrival rays.

The large amplitude eigen-ray arrivals around 0.6 ms delay are most relevant for determining the peak pressure. This ray pair is close to the optimal constructive spacing of $1/10$ ms for the 2.5 kHz center frequency signal, and the total interference result produces the largest peak pressures for this signal. The reference RFM solution, however, does not show the large peak pressures observed for the 2.5 kHz signal by the HKA. This over-prediction of the late arrivals is further demonstrated as Δx is increased and the differences between the RFM and HKA become marked.

2.4.2 Multiple source-receiver separations

To study the effect of lower surface grazing angles Δx was incremented in 50-m range steps from 50 to 1000 m. The surface wave position resulting the largest peak HKA arrival was identified for inter-range comparison. These HKA and RFM time series are presented in Fig.

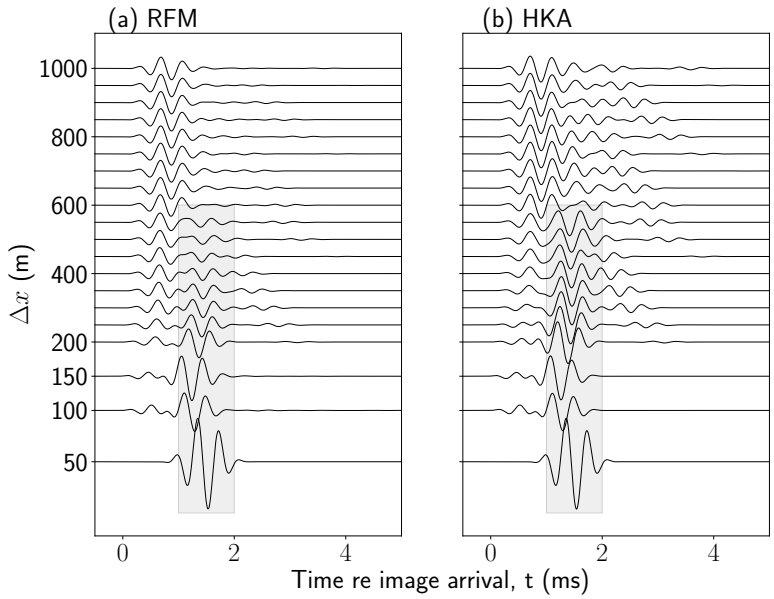

Figure 2.9: Cascade plot of acoustic pressure time series at wave time producing the largest arrival in the HKA solution for $f_c = 2.5$ kHz. Δx is increased by 50 m for each acoustic time series, while all other simulation parameters are the same as in Fig. 2.1: (a) RFM solution and (b) HKA solution. The delay times of the largest HKA arrivals are highlighted in grey for ranges where this is clearly associated with late arrival rays. The acoustic time series is first normalized in amplitude and delay to the image arrival, and then scaled by 40 for legibility. The vertical spacing for the 50, 100 and 150-m time series have been increased to improve legibility, while the rest of the time series have a constant offset of 50 m.

2.9. The eigen-rays for this wave position are shown in Fig. 2.8(b). The delay of the largest HKA arrivals is highlighted by a grey box for both solutions, and this corresponds to the delay highlighted in Fig. 2.8 after convolution with the source signal. The basic shape of the HKA result, Fig 2.9(b), remains consistent as Δx is varied from 200 m, with large late arrivals occurring up to 600-m Δx. The HKA time spread for the 2.5 kHz signal remains larger than 2 ms for all ranges, sometimes up to 4 ms. This is consistent with the late eigen-rays around 0.6 ms, Fig. 2.8(b), which reflect close to the receiver and show large amplitude for all ranges up to 600 m. Additionally, for Δx beyond 350-m, very late eigen-rays with about 1.5 ms delays are apparent which reflect from the surface near the source. The majority of the eigen-rays, occurring in the middle of the travel time curve, approach the flat surface travel time curve as range increases and

interfere to create an image source at long ranges.

The RFM solution in Fig. 2.9(a) agrees well with the HKA up to Δx of 200 m, when distinctions become apparent. The late arrivals fade with increasing Δx past 200-m and are hardly significant beyond 400 m. Additionally, eigen-rays with delays more than 1.5 ms do not appear significant in the RFM solution. Finally, beyond 600-m Δx the RFM is virtually indistinguishable from the image solution, while the HKA only approaches this result around 1000-m Δx. This result is consistent with the reflection coefficients in Fig. 2.5 which shows the 0-th RFM coefficient approaches 1 the angle of incidence approaches 0°, while other coefficients approach 0. The 0-th HKA coefficient also approaches 1 as the angle of incidence approaches 0°, but the negative Bragg orders approach non-zero values. The eigen-rays of Fig. 2.8 and the time series of Fig. 2.9 demonstrate that the HKA error seen in reflection coefficients at low grazing angles is the result of late arrival rays. These rays, reflecting of the surface near the source and receiver, are well modeled by the HKA for small Δx values, but become the dominant source of error for larger Δx values.

The error of the HKA compared to the RFM and the image solution is shown against range in Fig. 2.10. This error is calculated as the integral in time, t, of the absolute difference between two solutions for a fixed surface wave position. This result is then normalized by the image-source amplitude to remove the effect of spreading loss. There is little mismatch between the RFM and the HKA for Δx values up until 150 m. The error between the two solutions begins to increase sharply at this point, and the difference between the two solutions levels off around 300 m Δx. At 350-m and greater Δx, the simple image-source solution has less integrated absolute difference compared to the RFM. This suggests the image solution is preferred over the HKA at 350 m and beyond for the test scenario under consideration.

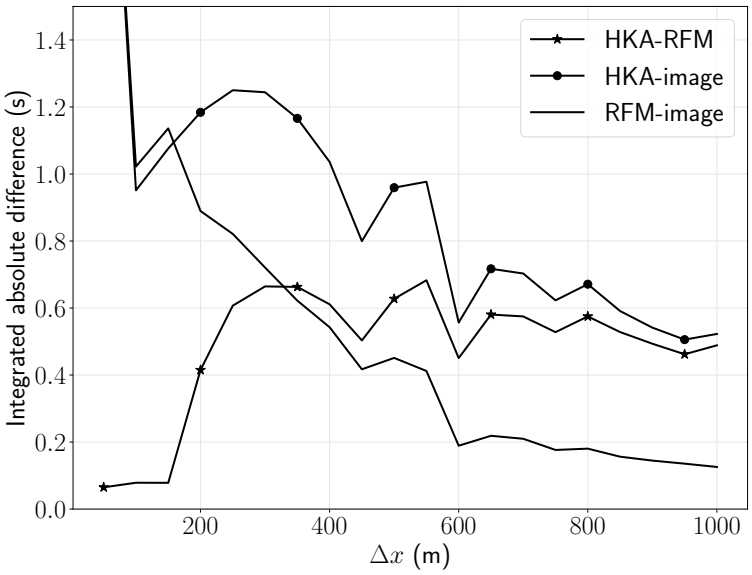

Figure 2.10: Absolute difference of acoustic pressure integrated over time (t) at the surface wave time (t_{wv}) of maximum HKA arrival. Comparisons are taken between: RFM and HKA, HKA and image-source, RFM and image-source. For each range, the RFM and HKA time series used in the integration are the same as those plotted in Fig. 2.9.

2.5 Summary

For sinusoidal surfaces (40-m wavelength, 20-m source and 10-m receiver depths) at short Δx (up to 150-m), HKA results agreed with reference RFM solutions. At moderate Δx (around 200 m), the HKA sometime over-estimated the peak pressure, dependent on the frequency of the signal tested. Eigen-ray interferences were used as an explanation for the frequency dependent HKA over-prediction. As the source-receiver x-separation was extended to longer ranges (past 200 m), the error of the HKA increased significantly at all frequencies. The HKA continued to predict large amplitude late arrival features up to 550-m Δx and significant acoustic time spread up to 1000-m Δx. In contrast, the RFM approached the image-source solution quickly for Δx past 350 m. After 350-m Δx the image-source approximation had less integrated mismatch with the reference RFM than the HKA.

This study used the RFM reference solution to inform the application of the more practical and flexible HKA. As Δx was extended to explore low grazing angles the HKA began to show

significant error. The range for which the HKA is an useful approximation extended for some distance past the point suggested by planewave reflection coefficients. When solving for acoustic scatter from monochromatic surface waves at short ranges, the HKA was found to be a useful method for modeling and understanding acoustic scatter in the time domain. The monochromatic surface solution modeled by the RFM is expected to give relevant bounds on experimental geometries for which the HKA result is accurate, and lend credence when using the approximation for more complicated scattering problems with the same geometries.

2.6 Acknowledgments

Chapter 2, in full, is a reprint of the material as it appears in the Journal of the Acoustical Society of America 2018, authored by; Edward L. Richards, H. C. Song and W. S. Hodgkiss. The dissertation/thesis author was the primary investigator and author of this paper. This research was supported by the Office of Naval Research under grants N00014-14-1-0459 and N00014-16-1-2476 and N00014-18-1-2123.

Bibliography

[1] E. I. Thorsos and S. L. Broschat, "An investigation of the small slope approximation for scattering from rough surfaces. Part I. Theory," *The Journal of the Acoustical Society of America*, vol. 97, no. 4, pp. 2082–2093, 1995.

[2] J. Senne, A. Song, M. Badiey, and K. B. Smith, "Parabolic equation modeling of high frequency acoustic transmission with an evolving sea surface," *The Journal of the Acoustical Society of America*, vol. 132, no. 3, pp. 1311–1318, 2012.

[3] R. S. Keiffer and J. C. Novarini, "A time domain rough surface scattering model based on wedge diffraction: Application to low-frequency backscattering from two-dimensional sea surfaces," *The Journal of the Acoustical Society of America*, vol. 107, no. 1, pp. 27–39, 2000.

[4] W. C. Meecham, "On the use of the Kirchhoff approximation for the solution of reflection problems," *Journal of Rational Mechanics and Analysis*, vol. 5, no. 2, pp. 323–334, 1956.

[5] S. P. Walstead and G. B. Deane, "Reconstructing surface wave profiles from reflected acoustic pulses," *The Journal of the Acoustical Society of America*, vol. 133, no. 5, pp. 2597–2611, 2013.

[6] S. P. Walstead and G. B. Deane, "Intensity statistics of very high frequency sound scattered from wind-driven waves," *The Journal of the Acoustical Society of America*, vol. 139, no. 5, pp. 2784–2796, 2016.

[7] Y. Choo, H. C. Song, and W. Seong, "Numerical study of three-dimensional sound reflection from corrugated surface waves," *The Journal of the Acoustical Society of America*, vol. 140, no. 4, pp. 2290–2296, 2016.

[8] Y. Choo, H. C. Song, and W. Seong, "Time-domain Helmholtz-Kirchhoff integral for surface scattering in a refractive medium," *The Journal of the Acoustical Society of America*, vol. 141, no. 3, pp. EL267–EL273, 2017.

[9] K. Williams, J. Stroud, and P. Marston, "High-frequency forward scattering from Gaussian spectrum, pressure release, corrugated surfaces. I. Catastrophe theory modeling," *The Journal of the Acoustical Society of America*, vol. 96, no. 3, pp. 1687–1702, 1994.

[10] E. I. Thorsos, "The validity of the Kirchhoff approximation for rough surface scattering using a Gaussian roughness spectrum," *The Journal of the Acoustical Society of America*, vol. 83, no. 1, pp. 78–92, 1988.

[11] E. Liszka and J. McCoy, "Scattering at a rough boundary – extensions of the Kirchhoff approximation," *The Journal of the Acoustical Society of America*, vol. 71, no. 5, pp. 1093–1100, 1982.

[12] E. I. Thorsos and D. R. Jackson, "Studies of scattering theory using numerical methods," *Waves in Random Media*, vol. 1, no. 3, pp. S165–S190, 1991.

[13] R. M. Oba, "Global boundary flattening transforms for acoustic propagation under rough sea surfaces," *The Journal of the Acoustical Society of America*, vol. 128, no. 1, pp. 39–49, 2010.

[14] D. H. Berman and J. S. Perkins, "Rayleigh method for scattering from random and deterministic interfaces," *The Journal of the Acoustical Society of America*, vol. 88, no. 2, pp. 1032–1044, 1990.

[15] R. Petit, L. Botten, M. Cadilhac, G. Derrick, D. Maystre, R. McPhedran, M. Neviere, and P. Vincent, *Electromagnetic Theory of Gratings*. Topics in Current Physics, Springer Berlin Heidelberg, 1980.

[16] A. T. Abawi, "The use of the virtual source technique in computing scattering from periodic ocean surfaces," *The Journal of the Acoustical Society of America*, vol. 130, no. 2, pp. 683–688, 2011.

[17] R. F. Millar, "On the Rayleigh assumption in scattering by a periodic surface," *Mathematical Proceedings of the Cambridge Philosophical Society*, vol. 65, no. 3, p. 773791, 1969.

[18] P. Beckmann and A. Spizzichino, "The scattering of electromagnetic waves from rough surfaces," *Norwood, MA, Artech House, Inc., 1987, 511 p.*, 1987.

[19] Y. Choo, W. Seong, and H. Song, "Emergence of striation patterns in acoustic signals reflected from dynamic surface waves," *The Journal of the Acoustical Society of America*, vol. 136, no. 3, pp. 1046–1053, 2014.

[20] M. Badiey, A. Song, and K. B. Smith, "Coherent reflection from surface gravity water waves during reciprocal acoustic transmissions," *The Journal of the Acoustical Society of America*, vol. 132, no. 4, pp. EL290–EL295, 2012.

[21] F. Jensen, W. Kuperman, M. Porter, and H. Schmidt, *Computational Ocean Acoustics*. Springer, New York, NY, 2011.

[22] J. Kaiser and R. Schafer, "On the use of the I0-sinh window for spectrum analysis," *IEEE Transactions on Acoustics, Speech, and Signal Processing*, vol. 28, pp. 105–107, February 1980.

[23] D. F. McCammon and S. T. McDaniel, "Application of a new theoretical treatment to an old problem; sinusoidal pressure release boundary scattering," *The Journal of the Acoustical Society of America*, vol. 78, no. 1, pp. 149–156, 1985.

[24] R. Holford, "Scattering of sound waves at a periodic, pressure-release surface: An exact solution," *The Journal of the Acoustical Society of America*, vol. 70, no. 4, pp. 1116–1128, 1981.

[25] K. Riley, M. Hobson, and S. Bence, *Mathematical Methods for Physics and Engineering: A Comprehensive Guide*. Cambridge University Press, Cambridge, UK, 2006.

[26] A. Oppenheim and R. Schafer, *Discrete-Time Signal Processing*. Pearson Education, 2010.

[27] R. F. Millar, "The Rayleigh hypothesis and a related least-squares solution to scattering problems for periodic surfaces and other scatterers," *Radio Science*, vol. 8, no. 8-9, pp. 785–796, 1973.

[28] D. F. McCammon, *An Evaluation of the Kirchhoff Approximation for Acoustic Plane Wave Reflection Coefficients from a Sinusoidal Boundary*. PhD thesis, The Pennsylvania State Universisty, 1984.

Chapter 3

Limited duration integral equation method for acoustic sea surface scatter calculations

This study describes the limited duration integral equation method (DIEM) for calculating broadband scatter from sea surfaces. The DIEM solves for surface scatter using a numerical integration of Green's theorem, the same solution framework used in the Helmholtz-Kirchhoff approximation (HKA). The DIEM replaces the HKA with a numerically calculated solution to a Helmholtz integral equation (HIE), a theoretically exact description of the surface scatter result. The limited duration approximation of the DIEM uses the spatiotemporal relationship of the time domain HKA to limit the spatial extent of HIE calculations. The DIEM results are confirmed for a one-dimensional sinusoidal surface using the exact Rayleigh-Fourier method (RFM), in a scenario where the HKA solution yields significant error. A sinusoidal surface was chosen for this comparison because the RFM requires periodic surfaces. The DIEM, however, is not limited to a specific surface type, making it a natural and computationally tractable solution for scatter studies.

3.1 Introduction

The modeling of broadband acoustic scatter from realistic sea surfaces is computationally prohibitive for many scenarios of practical interest, leading to the common use of approximate solutions. Scattering approximations include eigenrays,[1] the parabolic equation,[2] and the Helmholtz-Kirchhoff approximation (HKA).[3] Each approximate solution is useful for scattering calculations in the varied environments relevant to ocean acoustic studies, but these approximate results require verification using reference solutions. This study investigates the use of a limited duration integral equation method (DIEM) as a scatter reference solution that shares a common framework with the HKA and allows for general scatter surfaces. The DIEM is demonstrated for a one-dimensional surface with a line source for an example geometry that contrasts the DIEM with the HKA.

The DIEM and HKA both solve for surface scatter as an infinite surface integral using the

Green's theorem solution of the Helmholtz governing equation. The HKA uses an approximate form of Green's theorem integral, while the DIEM calculates the Green's theorem integrand using a Helmholtz integral equation (HIE). The HKA becomes less accurate for either low grazing angle scatter or steep surfaces.[4] This study uses a moderately sloped sinusoidal surface to focus on a low grazing angle propagation scenario, characterized by a large horizontal separation between the source and receiver relative to their depths.[5] The development of the DIEM is motivated by the inaccuracy of the HKA for transmission scenarios of importance to sea surface scatter studies, and the need for a reference solution that builds from the same framework as the HKA.

The DIEM numerically approximates the infinite spatial integral of the exact HIE after a spatial truncation, which results in truncation error.[6] While numerical solution of the HIE has been used in a number of narrowband scattering studies, typically mitigating the truncation error requires a modification of the problem setup. A spatial tapering of the source was introduced by Thorsos [7] to reduce the acoustic pressure incident on the truncation edges. Alternatively, Dawson and Fawcett [8] assumed a limited spatial extent of the surface deformations. Instead of modifying the incident pressure field or scattering surface profile, the DIEM mitigates the spatial truncation effects in broadband scatter results after a transformation into the time domain. The HKA is used to predict the arrival time of truncation effects in the DIEM time series, allowing for the temporal isolation of these effects after all significant scatter has occurred. Williams, Stroud and Marston [9] previously used the time domain to remove spatial truncation effects from HKA results, and the effectiveness of this approach is demonstrated here for DIEM solutions.

This study uses a sinusoidal scattering surface because it has an established reference solution, the Rayleigh-Fourier method (RFM).[10] The RFM uses the periodic structure of the surface to reduce scattering calculations to a single period, a procedure common to the larger class of grating methods.[11] The formulation of the DIEM does not place any restrictions on the scattering surface, however, and it is expected to be a valid reference solution for more general surface geometries than the periodic surfaces required for grating methods.

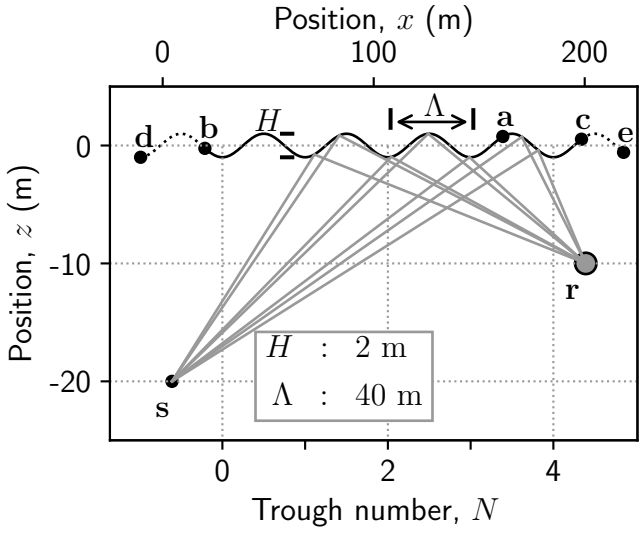

Figure 3.1: Test setup. The acoustic source is at 20-m depth, the receiver is at 10-m depth, with 200-m horizontal separation. The point **a** indicates a general location along the scattering surface. The points **b** and **c** are endpoints used in Green's theorem integration, Sec. 3.2.2. The endpoints, **d** and **e**, are specific to DIEM calculations and discussed in Sec. 3.3.2. Seven eigenrays, acoustic rays that obey specular reflection at the scattering surface, are plotted as gray lines. The trough number along the x-axis is introduced as the index of surface minima, measured from the origin (trough number 0 is at $x = 24.35$ m for wave phase $\zeta = 5.6$ rad).

Section 3.2 introduces the study test setup and acoustic governing equation. Green's theorem then is used to formulate the scatter solution as an infinite surface integral. Section 3.3 discusses the HKA, DIEM and RFM scatter solutions along with a description of the specific numerical implementation of each method. Section 3.4 discusses the calculation of HKA and DIEM scatter time series, and the limited duration approximation used to truncate spatial integral lengths of Green's theorem. Section 3.5 demonstrates that the DIEM time series is virtually identical to that of the exact RFM solution. Intermediate DIEM results then are used to illustrate some shortcomings of the HKA at low grazing angles.

3.2 Problem statement

We consider the test geometry illustrated in Fig. 3.1 that previously was shown to yield significant HKA error for acoustic frequencies around 2.5 kHz.[5] The scattering surface, $\eta(x)$, is

defined as

$$\eta(x) = \frac{H}{2}\cos\left(\frac{2\pi x}{\Lambda} + \zeta\right), \tag{3.1}$$

where wave height, $H = 2$ m, and wave length, $\Lambda = 40$ m. Unless otherwise stated, all results use a wave phase, $\zeta = 5.6$ rad, which leads to a large amplitude arrival in HKA scatter time series.

The DIEM, HKA and RFM scattering solutions considered in this study are derived from the Helmholtz governing equation and a pressure release boundary condition. The Helmholtz equation assumes a frozen surface, which is considered appropriate for sea surface scatter studies with short duration transmissions.[3] Section 3.4 discusses scatter time series using a specific short duration transmission that gives an estimate of the scatter impulse response over a finite bandwidth. While the specifics of a long duration transmission simulation are not discussed further, such a study could account for the temporal evolution of the physical surface using a sequence of frozen surface impulse responses.

3.2.1 Governing Helmholtz equation

The pressure field from a line source in the acoustic volume satisfies the governing two-dimensional Helmholtz equation,

$$(\nabla^2 + k^2)\Phi(\mathbf{r}) = \delta(\mathbf{r} - \mathbf{s}), \tag{3.2}$$

where $\mathbf{s}$ and $\mathbf{r}$ correspond to the source and receiver positions, respectively. The medium is assumed to have a constant sound speed $c = 1500$ m/s. The wavenumber, k, is defined as $2\pi f/c$, where f is the acoustic frequency.

Following Meecham,[12, Meecham] the pressure field is split into a sum of two fields,

$$\Phi(\mathbf{r}) = \Phi_{inc}(\mathbf{r}) + \Phi_{sca}(\mathbf{r}). \tag{3.3}$$

The incident pressure field, Φ_{inc}, is defined by the Green's function,

$$G(\mathbf{r},\mathbf{s}) = \Phi_{inc}(\mathbf{r}) = \frac{i}{4} H_0^{(1)}(k\|\mathbf{r}-\mathbf{s}\|), \tag{3.4}$$

where $H_0^{(1)}$ is the zero-th order Hankel function of the first kind. The pressure field, Φ_{sca}, is the scatter from the surface due to the incident pressure field.

A pressure release boundary condition is used for the scattering surface of Eq. (3.1). A half-space model is assumed below the scattering surface. The position vector, $\mathbf{a}$, shown in Fig. 3.1, indicates a general position along the scattering surface. The pressure release boundary condition is

$$\Phi_{sca}(\mathbf{a}) = -\Phi_{inc}(\mathbf{a}). \tag{3.5}$$

The governing equation of Eq. (3.2) and the boundary condition of Eq. (3.5) fully determine the scattered pressure at the receiver, $\Phi_{sca}(\mathbf{r})$.

3.2.2 Green's theorem

Green's theorem is used to formulate the solution to the Helmholtz governing equation as a contour integration. This study uses the Green's function proposed by Meecham,[12] and an integral notation similar to DeSanto,[13]

$$\Phi(\mathbf{r}) = \Phi_{inc}(\mathbf{r}) + \int_S dx \, \frac{\partial}{\partial n}\Phi(\mathbf{a}) \; G(\mathbf{r},\mathbf{a}), \tag{3.6}$$

where S denotes an infinite integral along the pressure release surface. The $G(\mathbf{r},\mathbf{a})$ term is the Green's function of Eq. (3.4), which describes the response at the receiver $\mathbf{r}$ to a source at surface position $\mathbf{a}$, with strength $\partial\Phi(\mathbf{a})/\partial n$. The infinitesimal of the integral is taken along the x-axis, while all functions are evaluated at the scattering surface position that corresponds to x. The normal derivative operator, $(\vec{n}\cdot\nabla)$, is defined using a non-unit normal vector, $\vec{n} = [-\partial\eta(x)/\partial x, 1]$.

The scattered pressure, $\Phi_{sca}(\mathbf{r})$, is the integral term in Eq. (3.6). The DIEM and HKA methods both solve for the scattered pressure numerically by rectangular quadrature, but use different values of $\partial\Phi(\mathbf{a})/\partial n$ in this calculation. Numerical solution for the scattered pressure introduces the finite spatial integration endpoints, **b** and **c**, shown in Fig. 3.1,

$$\Phi_{sca}(\mathbf{r}) \approx \int_{\mathbf{b}}^{\mathbf{c}} dx \, \frac{\partial}{\partial n}\Phi(\mathbf{a}) \; G(\mathbf{r},\mathbf{a}). \tag{3.7}$$

The truncation error of this approximation is discussed for time series scatter calculations in Sec. 3.4.

3.3 Solution methods

Three different solution methods for the normal derivative of the pressure field at the surface, $\partial\Phi(\mathbf{a})/\partial n$, are discussed in this section: HKA, DIEM and RFM. The HKA uses a closed form approximation for $\partial\Phi(\mathbf{a})/\partial n$ which leads to an analytic expression for the scattered pressure. The DIEM computes $\partial\Phi(\mathbf{a})/\partial n$ numerically based on an integral equation, with a spatial integration interval selected by a convergence analysis. The RFM, an exact solution that incorporates the periodicity of the surface, is used to validate the integral equation calculation of the DIEM.

3.3.1 HKA

This derivation of the HKA begins with the Kirchhoff approximation,[12] which enforces a local pressure release boundary condition at each point,

$$\frac{\partial}{\partial n}\Phi^{HKA}(\mathbf{a}) = 2\frac{\partial}{\partial n}\Phi_{inc}(\mathbf{a}), \tag{3.8}$$

where $\Phi_{inc} = G(\mathbf{a},\mathbf{s})$ according to Eq. (3.4). The doubling of $\partial\Phi^{HKA}(\mathbf{a})/\partial n$, assumed by the Kirchhoff approximation, is an exact result for flat scattering surfaces with the pressure release boundary condition of Eq. (3.5).

The Kirchhoff approximation is substituted into Eq. (3.7) to give the HKA,

$$\Phi^{HKA}_{sca}(\mathbf{r}) \approx -\frac{1}{4\pi}\int_{\mathbf{b}}^{\mathbf{c}} dx\ \frac{\big(\mathbf{a}-\mathbf{s}\big)\cdot\vec{n}}{\big|\mathbf{a}-\mathbf{s}\big|}\ \frac{\exp\Big(ik\Big(\big|\mathbf{a}-\mathbf{s}\big|+\big|\mathbf{r}-\mathbf{a}\big|\Big)\Big)}{\sqrt{\big|\mathbf{a}-\mathbf{s}\big|\ \big|\mathbf{r}-\mathbf{a}\big|}}. \tag{3.9}$$

The distances between the source, receiver and surface are assumed long enough to use the large argument asymptotic of the Hankel function. The significant approximation of Eq. (3.9) is instead related to the positions of the endpoints, **b** and **c**. The errors caused by the specific placements of **b** and **c** are discussed in Sec. 3.4.2 using time domain results.

3.3.2 DIEM

The DIEM uses a Fredholm integral equation of the first kind to solve for the pressure field at the surface, referred to as the Helmholtz integral equation (HIE). The HIE is the result of the limiting process of bringing the receiver in Eq. (3.6) to the scattering surface itself,

$$\Phi_{sca}(\mathbf{a}) = \int_{S} dx'\ \frac{\partial}{\partial n}\Phi(\mathbf{a}')\ G\big(\mathbf{a},\mathbf{a}'\big) = -\Phi_{inc}(\mathbf{a}), \tag{3.10}$$

where the prime notation indicates a dummy variable of integration. The $G(\mathbf{a},\mathbf{a}')$ term is the Green's function of Eq. (3.4), which describes the acoustic response at surface point **a** to a source at surface position $\mathbf{a}'$, with strength $\partial\Phi(\mathbf{a}')/\partial n$.

The DIEM approximates Eq. (3.10) with a finite interval integration,

$$\int_{\mathbf{d}}^{\mathbf{e}} dx'\ \frac{\partial}{\partial n}\Phi^{DIEM}(\mathbf{a}')\ G\big(\mathbf{a},\mathbf{a}'\big) \approx -\Phi_{inc}(\mathbf{a}), \tag{3.11}$$

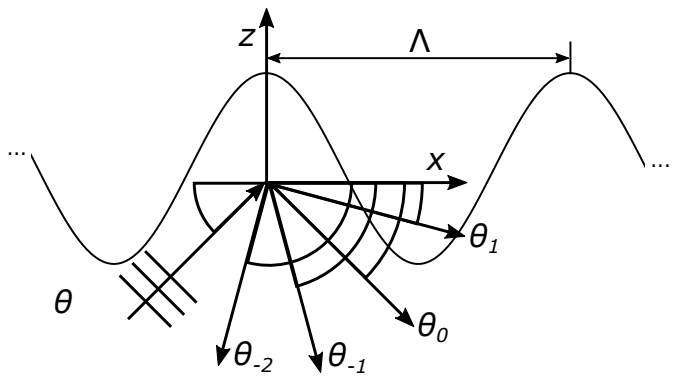

Figure 3.2: Rayleigh expansion for plane waves scattered from a periodic surface with an incident plane wave. A single up-going incident plane wave gives rise to a finite number of scattered plane waves that propagate downward. The angle θ_0 is the specular reflection direction, where $\cos(\theta) = \cos(\theta_0)$.

which is discretized into a matrix equation to solve for the unknown term, $\partial\Phi^{DIEM}(\mathbf{a})/\partial n$, following Thorsos.[7]

The positions of endpoints **d** and **e** are determined after specifying the positions of endpoints **b** and **c**, used to calculate the pressure at the receiver,

$$\Phi^{DIEM}_{sca}(\mathbf{r}) \approx -\frac{1}{4\pi}\int_{\mathbf{b}}^{\mathbf{c}} dx\, \frac{\partial}{\partial n}\Phi^{DIEM}(\mathbf{a})\frac{\exp\left(ik|\mathbf{r}-\mathbf{a}|\right)}{\sqrt{|\mathbf{r}-\mathbf{a}|}}. \tag{3.12}$$

The placement of endpoints **b** and **c** is made with the aid of the time domain HKA, discussed in Sec. 3.4.2. A convergence analysis then determines the integration length of Eq. (3.11) required to correctly compute $\partial\Phi(\mathbf{a})/\partial n$ between endpoints **b** and **c**. As described in Sec. 3.5.2, a small extension of the integration length of Eq. (3.12) is needed for calculation of Eq. (3.11), illustrated by the position of endpoints **d** and **e** in Fig. 3.1.

3.3.3 RFM

Grating methods, like the RFM, require both a plane wave acoustic source and a periodic surface, and are solved over a single periodic length of the surface.[11] Grating methods solve for

the amplitudes of the plane and evanescent waves predicted by the Rayleigh expansion shown in Fig. 3.2, which have propagation angles,

$$\cos(\theta_q) = \cos(\theta) + \frac{2\pi q}{\Lambda k}. \tag{3.13}$$

The angles of the scattered plane waves are real if $|\cos(\theta) + 2\pi q/(\Lambda k)| < 1$, indicating a propagating wave. Imaginary values of θ_q indicate an evanescent wave, decaying exponentially as $z \to -\infty$.

While the Rayleigh expansion gives the angles of the scattered waves, it does not specify their amplitudes, *i.e.* the reflection coefficients. The RFM is used to determine the reflection coefficients because of its straightforward formulation and implementation, following Richards *et al.*[5]. Although the RFM is not expected to give the correct pressure field at all positions in the acoustic medium for general periodic surfaces, the RFM is valid inside the medium for sinusoidal surfaces with limited slope.[14] The RFM sinusoidal slope limit ($\pi H/\Lambda \leq 0.448\ldots$) is considered sufficient for scattering surfaces approximating ocean swell, which allows for calculation of the surface field $\partial\Phi^{RFM}(\mathbf{a})/\partial n$.

The wave number synthesis discussed in the appendix computes line source results from plane wave source calculations,

$$\begin{aligned}\frac{\partial}{\partial n}\Phi^{RFM}(\mathbf{a}) = \frac{\partial}{\partial n}\Phi_{inc}(\mathbf{a}) - \frac{i}{4\pi}\sum_{q=l}^{u}\int_C d\theta\, R_q(\theta)\, \left(\sin(\theta_q) + \cos(\theta_q)\frac{d\eta}{dx}(x)\right) \\ \exp\left[ik\big(\cos(\theta_q)(x-x_s) - \sin(\theta_q)(\eta(x)-z_s)\big)\right],\end{aligned} \tag{3.14}$$

where $R_q(\theta)$ is the reflection coefficient of the q-th plane wave for an incident plane wave of angle θ.

The scattered pressure at a receiver similarly is computed as

$$\Phi_{sca}^{RFM}(\mathbf{r}) = -\frac{i}{4\pi}\sum_{q=l}^{u}\int_{C} d\theta\, R_q(\theta)\exp\left[ik\big(\cos(\theta_q)(x_r - x_s) + \sin(\theta_q)|z_r + z_s|\big)\right]. \tag{3.15}$$

The limited integration length relevant to the wave number integration contour C, see appendix, combined with the limited number of relevant Bragg orders, makes the solutions of Eq. (3.14) and (3.15) computationally tractable expressions for the exact scattered pressure field.

3.4 Scatter time series calculations

Scatter results are calculated as bandlimited impulse response (IR) estimates, which are scatter time series for short time pulse transmissions. Section 3.4.1 describes the calculation of time series from frequency domain scatter solutions. Section 3.4.2 introduces a minimum travel time description of the scatter time series, along with the time domain HKA. Section 3.4.3 uses the minimum travel time to relate limited spatial integration lengths in Green's theorem calculations to an arrival time for the truncation error. The travel time description models the truncation error as arrivals from the edges of Green's theorem integrations, and the edge arrivals are removed from the scatter IR to estimate the infinite scattering surface result.

3.4.1 Scatter impulse response estimates

Estimates of the IR are made over a finite band of frequencies centered at $f_c = 2.5$ kHz. A windowed four-cycle sinusoid is used as a transmission pulse that is both short in time and limited in bandwidth,

$$s(t) = w(t - 2/f_c)\sin(2\pi f_c t), \tag{3.16}$$

where $w(t)$ is a Kaiser-Bessel window with design parameter $\alpha = 2.5\ \pi$ and width $\tau = 4/f_c$.[15] The transmitted signal is plotted in Fig. 3.3, along with its frequency transform, $S(f)$. IR

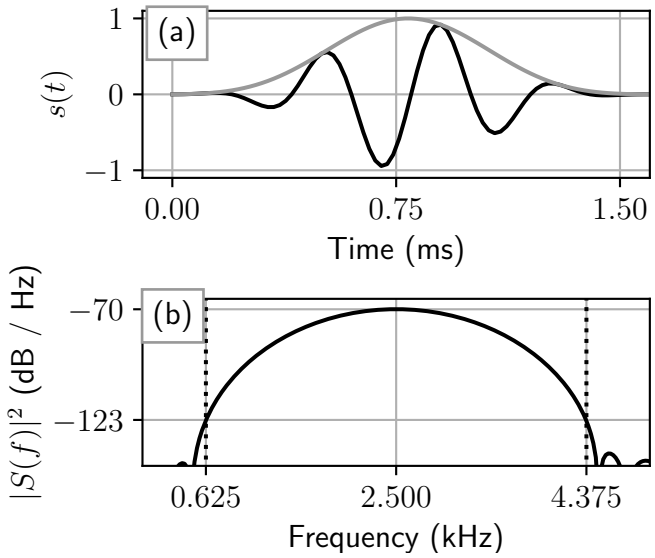

Figure 3.3: Transmitted signal: (a) time domain, (b) frequency domain. Transmitted pulse signal is a tapered four-cycle sinusoid, plotted as black line. The envelope of the transmitted pulse is plotted as a gray line, and has a maximum value at 0.78 ms. Scatter calculations are performed between 0.625 kHz and 4.375 kHz.

calculations use $S(f)$ and the inverse Fourier transform, $\mathcal{F}^{-1}$,

$$p_{sca}(\mathbf{r},t) = \mathcal{F}^{-1}\Big\{\Phi_{sca}(\mathbf{r},f)S(f)\Big\} = \int_{-\infty}^{\infty} df\, \exp(i2\pi ft)\, \Phi_{sca}(\mathbf{r},f)S(f). \tag{3.17}$$

The frequency band between 0.625 to 4.375 kHz (see Fig. 3.3) is used in the calculations shown in Sec. 3.5.

While the IR for RFM calculations is computed directly from the frequency domain result, the HKA and DIEM solutions apply the inverse Fourier transform to Green's theorem,

$$p_{sca}(\mathbf{r},t) = \int_S dx\ \mathcal{F}^{-1}\left\{\frac{\partial}{\partial n}\Phi(\mathbf{a},f)\ G(\mathbf{r},\mathbf{a},f)S(f)\right\} = \int_S dx\ v(\mathbf{a},t), \tag{3.18}$$

where the order of integration is interchanged. The function, $v(\mathbf{a},t)$, is introduced in the right-hand expression as the time domain integrand of Green's theorem for the transmitted pulse, $s(t)$.

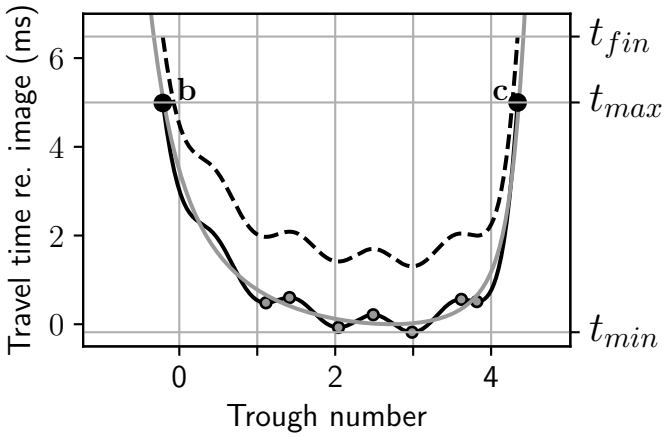

Figure 3.4: Minimum travel time curve, $\tau(\mathbf{a})$, plotted as a solid black line for the experimental setup of Fig. 3.1. Time is referenced to the image, or flat surface reflection, arrival time. The plot of $\tau(\mathbf{a})$ is terminated at the endpoints of Green's theorem integrations, **b** and **c**. Stationary points, local extrema of $\tau(\mathbf{a})$, are drawn as grey circles. The flat surface travel time, $\tau_0(x)$, is shown as the solid gray line with a single minima at 0 ms. The dashed curve shows the HKA prediction for the final arrival time, and is separated from $\tau(\mathbf{a})$ by the duration of the transmitted signal (~1.5 ms). Three time limits used in IR calculations are indicated with horizontal lines, t_{min}, t_{max} and t_{fin}, for the minimum, maximum and final time, respectively.

3.4.2 Minimum travel time and the time domain HKA

The time domain integrand of Green's theorem, $v(\mathbf{a},t)$, can be transformed analytically into the time domain for the HKA. In the HKA formulation of Eq. (3.9), the exponential phase function is the only frequency dependent term, and it represents a delay,

$$p_{sca}^{HKA}(\mathbf{r},t) = \int_S dx\, v^{HKA}(\mathbf{a},t) = -\frac{1}{4\pi}\int_S dx\, \frac{(\mathbf{a}-\mathbf{s})\cdot\vec{n}}{|\mathbf{a}-\mathbf{s}|}\, \frac{s\big(t-\tau(\mathbf{a})\big)}{\sqrt{|\mathbf{a}-\mathbf{s}|\;|\mathbf{r}-\mathbf{a}|}}. \tag{3.19}$$

An equality indicates the infinite surface integral gives the complete HKA result in the far-field, in contrast to Eq. (3.9) which was an approximate formulation with finite spatial boundaries.

The single arrival from each surface position in Eq. (3.19) is a scaled copy of the source transmission, $s(t)$. The arrival delay is

$$\tau(\mathbf{a}) = \frac{|\mathbf{a}-\mathbf{s}|+|\mathbf{r}-\mathbf{a}|}{c}, \tag{3.20}$$

which is the minimum travel time for paths that include the source, receiver and a single surface position $\mathbf{a}$. The solid black line in Fig. 3.4 shows $\tau(\mathbf{a})$ for the experimental setup of Fig. 3.1. The solid gray line in Fig. 3.4 is the travel time curve for a flat surface, introduced as $\tau_0(x)$. The travel time curves are referenced to the delay of the flat surface reflection, $\tau_{img} = r_{img}/c$, where r_{img} is the distance from the image source to the receiver. While the sinusoidal surface modifies the travel time from the flat surface result, the bowl-like shape is similar for both curves, with the similarity increasing along the bowl walls.

All positions along the scattering surface contribute to the scattered time series according to Eq. (3.19), but most of these arrivals interfere destructively. The dominant constructive interference can be predicted using first-order stationary phase analysis [9] of Eq. (3.19). Stationary phase analysis of the HKA predicts that each of the stationary points, grey circles in Fig. 3.4, leads to an eigen-ray contribution. Each eigen-ray, the gray paths in Fig. 3.1, obeys specular reflection at the surface.

The stationary points for $\tau(\mathbf{a})$ are clustered toward the center of the travel time curve of Fig. 3.4, with wave troughs and crests associated with local minima and maxima, respectively. The reduced sensitivity of $\tau(\mathbf{a})$ to the wave shape along the edges of the travel time curve restricts eigen-rays spatially to the region between trough numbers 1 and 4, and temporally to within 1 ms of the image arrival time. The eigen-ray analysis indicates clear spatial and temporal limits on the scatter solution, suggesting that a limited spatial integration of Green's theorem is sufficient to describe the scatter solution.

The scatter IR of the HKA is calculated numerically with Eq. (3.19), and the results of stationary phase analysis are not further developed here. One advantage to the numerical solution of the HKA is that it allows for a direct comparison with the DIEM of Green's theorem calculations, Eq. (3.18). Additionally, numerical HKA calculations avoid the shadow zones and caustic features of eigen-ray propagation solutions,[16] which require higher order stationary phase corrections.[9] The eigen-ray analysis of the HKA does provide an intuitive description of

the scatter results, however, and the distinct arrival features of eigen-rays are apparent in both the HKA and DIEM results shown in Sec. 3.5.

3.4.3 Limited surface spatial integration

Stationary phase analysis of the HKA predicts that scatter IRs have a finite duration, with contributions arriving from a limited region of the surface. The spatiotemporal relationship of the minimum travel time, $\tau(\mathbf{a})$ of Eq. (3.20), further relates all scatter IRs with a finite duration to a finite spatial interval of the scattering surface. However, significant truncation error is introduced when Green's theorem calculations are restricted to just the relevant surface interval determined by the scatter IR duration. The time domain HKA is used to model the truncation error as edge arrivals following Williams (in discussion of Eq. 7),[9] with the edge arrival times determined by the positions of the integration endpoints. The times of the edge arrivals are used to isolate the truncation error so that it occurs after all physical scatter arrivals, and the error effectively is removed by considering only the limited duration of the calculated IR, up to the edge arrivals, to be valid.

The exact solution for the IR, Eq. (3.18), contains scatter arrivals between t_{min} and t_{max}, shown in Fig. 3.4: t_{min} is the global minimum of $\tau(\mathbf{a})$ and t_{max} is chosen so the IR effectively is 0 for $t \geq t_{max}$. For a choice of t_{max}, the finite spatial interval used in Green's theorem calculations is

$$p_{sca}(\mathbf{r},t) \approx \int_{\mathbf{b}}^{\mathbf{c}} dx\, v(\mathbf{a},t), \tag{3.21}$$

where the endpoints of integration are selected so that $\tau(\mathbf{b}) = \tau(\mathbf{c}) = t_{max}$. All positions with $\tau(\mathbf{a})$ less than t_{max} are included in the spatial integration interval between $\mathbf{b}$ and $\mathbf{c}$, and so all of $v(\mathbf{a},t)$ before t_{max} is included in the scatter IR calculation. For all scatter IR calculations considered in this study, $t_{max} = \tau_{img} + 5$ ms. The selection of t_{max} is made with HKA scatter IR calculations, Sec. 3.5.1.

The finite spatial integration interval of Eq. (3.21) introduces computational artifacts in the scatter IR, edge arrivals that begin at t_{max} and end by a final time, t_{fin}. The value of t_{fin} is modeled with $v^{HKA}(\mathbf{a},t)$, Eq. (3.19). For each surface postion, $v^{HKA}(\mathbf{a},t)$ begins at $\tau(\mathbf{a})$ and extends for the duration of $s(t)$, ending at the dashed line in Fig. 3.4. The latest arrivals in the HKA scatter IR calculations are the endpoint contributions $v^{HKA}(\mathbf{b},t_{fin})$ and $v^{HKA}(\mathbf{c},t_{fin})$, where t_{fin} is t_{max} plus the duration of $s(t)$.

To compute the scatter IR, the DIEM uses the HKA estimate of t_{max} and t_{fin} to isolate and remove edge arrivals. The DIEM scatter IR are calculated between t_{min} and t_{fin} with a discrete Fourier transform approximation of Eq. (3.18). The calculated results then are limited in duration to t_{max}, with the IR set to 0 for $t \geq t_{max}$, which removes the edge arrivals from the calculated scatter IR.

The DIEM solution for $v(\mathbf{a},t)$ includes multiple scatter effects not modeled by the HKA that may result in time extensions past the last non-zero time of $v^{HKA}(\mathbf{a},t)$.[17] Comparison of the DIEM and HKA results for $v(\mathbf{a},t)$ in Sec. 3.5.3 shows that time extensions from multiple scatter are small for the surface under study, and that the HKA estimates for t_{max} and t_{fin} are sufficient for DIEM scatter IR calculations.

3.5 Results

A description of the DIEM solution method for the specific test setup of Fig. 3.1 is presented along with comparisons to HKA and RFM results. Section 3.5.1 describes the determination of the Green's theorem integration length from HKA estimates of t_{max}. Section 3.5.2 computes DIEM solutions for $\partial\Phi(\mathbf{a})/\partial n$ over the finite surface length identified by t_{max}, and compares the result to the HKA and RFM. Section 3.5.3 calculates the scatter IR from solutions of $\partial\Phi(\mathbf{a})/\partial n$, and demonstrates that the DIEM result essentially is the same as the RFM.

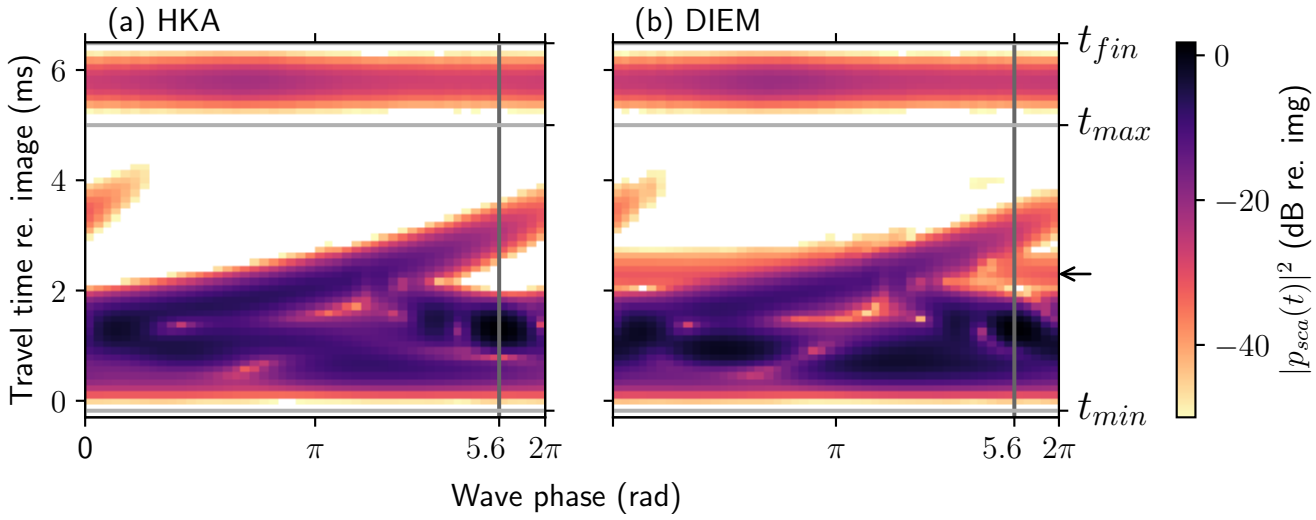

Figure 3.5: Envelope of the scatter time series, $p_{sca}(t)$, over a surface wave phase cycle: (a) HKA and (b) DIEM. Vertical lines mark the wave phase of Fig. 3.1, horizontal lines mark the time bounds t_{min}, t_{max} and t_{fin} introduced in Fig. 3.4. Arrivals after t_{max} and before t_{fin} are the edge arrivals of generated by the endpoints **b** and **c** of the spatial integral in Eq. (3.21). While the DIEM and HKA solutions have different amplitudes, only one significant arrival in the DIEM solution is not predicted by the HKA, a small amplitude arrival marked with the arrow at 2.3 ms in panel (b).

3.5.1 Estimates of t_{max}

The integration length used in Green's theorem calculations of Eq. (3.21) is determined with a value of t_{max} that includes all arrivals in the HKA IR. The value of t_{max} sufficient for the HKA solution is decided by computing the scatter time series, $p_{sca}^{HKA}(\mathbf{r},t)$, over an entire surface wave cycle and finding the latest scatter arrival. Figure 3.5 compares the time domain structure of the HKA to the DIEM solution. Note that the DIEM does not have any late arrivals that are not apparent in the HKA, and this similarity of arrival structure indicates that a choice of t_{max} made with the HKA scatter solutions is appropriate for DIEM calculations as well.

The envelope of the scatter time series, $p_{sca}(\mathbf{r},t)$, is plotted as intensity in Fig. 3.5, with the HKA and DIEM solutions shown in panels (a) and (b), respectively. The magnitude is referenced to the envelope maximum of the image arrival, $|p_{img}(\mathbf{r})| = (4\pi)^{-1}\sqrt{c/(f_c\, r_{img})}$, where r_{img} is the distance from the image source to the receiver. Time, t, progresses along the

vertical axis, with the origin set at the image arrival time, $t_{img} = r_{img}/c$. The arrival structure of $p_{sca}(\mathbf{r},t)$ depends significantly on the surface wave phase, which progresses along the bottom axis. Vertical lines mark the surface wave phase value used for the test setup of Fig. 3.1.

Calculations of $p_{sca}(\mathbf{r},t)$ are made with Eq. (3.21), where the endpoints **b** and **c** of the spatial integral are determined using $t_{max} = 5$ ms, shown in Fig. 3.4. Physical scatter is bounded by the horizontal lines at t_{min} and t_{max}. The edge arrivals from the finite spatial integration of Green's theorem are apparent in both solutions between t_{max} and t_{fin}. In addition to the edge arrivals, the HKA solution largely predicts the physical arrival structure of the DIEM. The one arrival not seen in the the HKA is the small amplitude arrival at 2.3 ms, a result of multiple scatter effects not modeled by the HKA.[17] The similarity of arrival structure means that the most significant differences occur in the amplitude of scatter arrivals, discussed in Sec. 3.5.3.

3.5.2 Solutions for $\partial\Phi(\mathbf{a})/\partial n$

The function $\partial\Phi(\mathbf{a})/\partial n$ is used by the Green's theorem integration of Eq. (3.7) to calculate the scatter pressure at the receiver. The HKA uses an analytic approximation for $\partial\Phi(\mathbf{a})/\partial n$, Eq. (3.8), while the DIEM computes it numerically over a limited spatial interval of the scattering surface, Eq. (3.11). The value of t_{max}, identified in Sec. 3.5.1, determines the surface interval for the computation of $\partial\Phi(\mathbf{a})/\partial n$ according to the discussion of Sec. 3.4.3. The comparisons shown in Fig. 3.6 are made at the center frequency, $f_c = 2.5$ kHz. Solutions for $\partial\Phi(\mathbf{a})/\partial n$ are normalized by the normal derivative of the pressure for a flat surface, $|\partial\Phi_0(x)/\partial n|$.

The agreement between the HKA and reference RFM solution of $\partial\Phi(\mathbf{a})/\partial n$ depends on the distance along the surface from $x = 0$. The HKA is similar to the RFM up to the first wave trough where the two solutions begin to diverge, consistent with the low grazing angle limitations of the HKA.[7] However, the HKA continues to share many features of the RFM solution throughout the surface length.

The local grazing angle of the incident pressure largely determines the normalized magni-

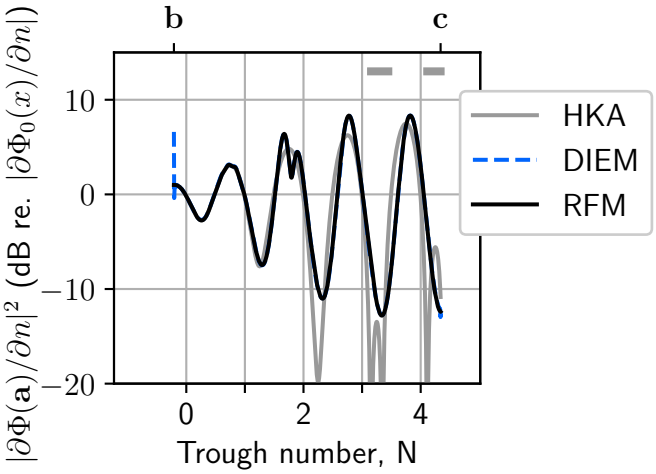

Figure 3.6: Comparison of $\partial\Phi(\mathbf{a})/\partial n^2$ between the HKA, DIEM, and RFM at $f_c = 2.5$ kHz. The interval across the surface for comparison is between the positions **b** and **c**, indicated on the top axis. The endpoints **d** and **e**, used in DIEM calculations of Eq. (3.11), are placed at positions **b** and **c**, which leads to significant error at the endpoints. Areas of the surface where straight line paths from the source to the surface are blocked are indicated with thick gray dashes above the results.

tude of $\partial\Phi(\mathbf{a})/\partial n$, shown in Fig. 3.6. For the HKA of Eq. (3.8), $\partial\Phi(\mathbf{a})/\partial n$ is directly proportional to the cosine of the source grazing angle. The wave profile increases the grazing angle on the source side of each wave trough and decreases it on the far side, leading to maxima and minima in $\partial\Phi(\mathbf{a})/\partial n$, respectively. Very low grazing angles reduce the amplitude of the cosine term to the limit of 0 amplitude, which leads to the deep HKA minima in Fig. 3.6. These amplitude minima are less extreme in the RFM solution, where diffraction prevents the deep nulls of the HKA.

Source shadowing corrections, which set the HKA solution for $\partial\Phi(\mathbf{a})/\partial n$ to 0 when incident rays are blocked from the source, are sometimes proposed as an intuitive improvement for the HKA.[18] Shadow zones occur when rays paths from the source to the surface are blocked by other portions of the surface, and are indicated with two grey dashes in Fig. 3.6. The shadow zones largely predict the location of the RFM minima, although a deep minimum that occurs after trough 2 is not associated with a shadow zone. The HKA, however, already underestimates the amplitude of the RFM in all shadow regions. Thus, the HKA accuracy is not expected to improve

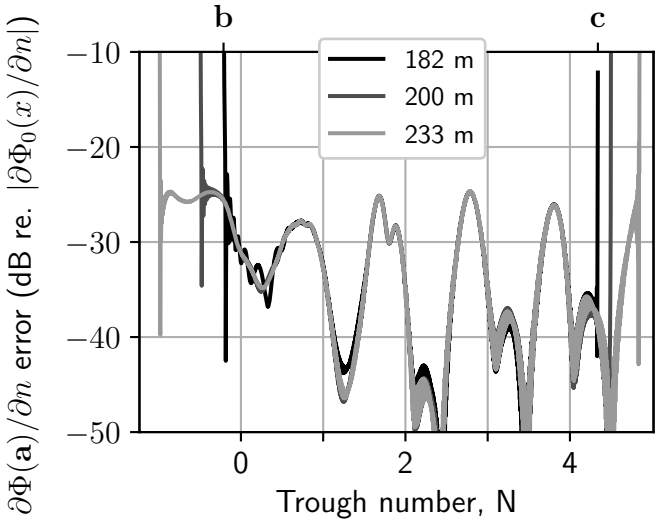

Figure 3.7: Error of $\partial\Phi^{DIEM}(\mathbf{a})/\partial n$ for different integration lengths of Eq. (3.11). The three integration lengths, 182, 200 and 233 m, correspond to a minimum travel time at the endpoints **d** and **e** of 5, 10 and 25 ms. Comparisons are made between endpoints **b** and **c**, indicated on the top axis.

with shadowing corrections, consistent with the shadowing study results of Holliday *et al.*[19]

The DIEM agrees with the RFM except at the edges of Fig. 3.6, which is more apparent at **b** than **c**. The mismatch primarily is because the DIEM result was calculated with the HIE endpoints, **d** and **e** in Eq. (3.11), collocated with **b** and **c**. A convergence analysis of $\partial\Phi(\mathbf{a})/\partial n$ between the endpoints **b** and **c** determines the extended spatial interval used for Eq. (3.11) calculations, which is shown in Fig. 3.7.

The RFM solution is used to compute the absolute error of $\partial\Phi^{DIEM}(\mathbf{a})/\partial n$ for different positions of the endpoints **d** and **e** in Eq. (3.11), shown in Fig. 3.7. The error of $\partial\Phi^{DIEM}(\mathbf{a})/\partial n$ is calculated by subtracting the RFM result for $\partial\Phi(\mathbf{a})/\partial n$, and the absolute value of the mismatch is normalized by $|\partial\Phi_0(x)/\partial n|$. The endpoints **d** and **e** are placed according to $\tau(\mathbf{d}) = \tau(\mathbf{e}) = t_{max}$, for t_{max} values of 5, 10 and 25 ms. This leads to integration lengths in Eq. (3.11) of 182, 200 and 233 m, respectively, and this extended integration interval is indicated in Fig. 3.1. While the 182 m integration length leads to significant error near endpoints **b** and **c**, the integration lengths of 200 and 233 m essentially have the same error between points **b** and **c**. The convergence analysis

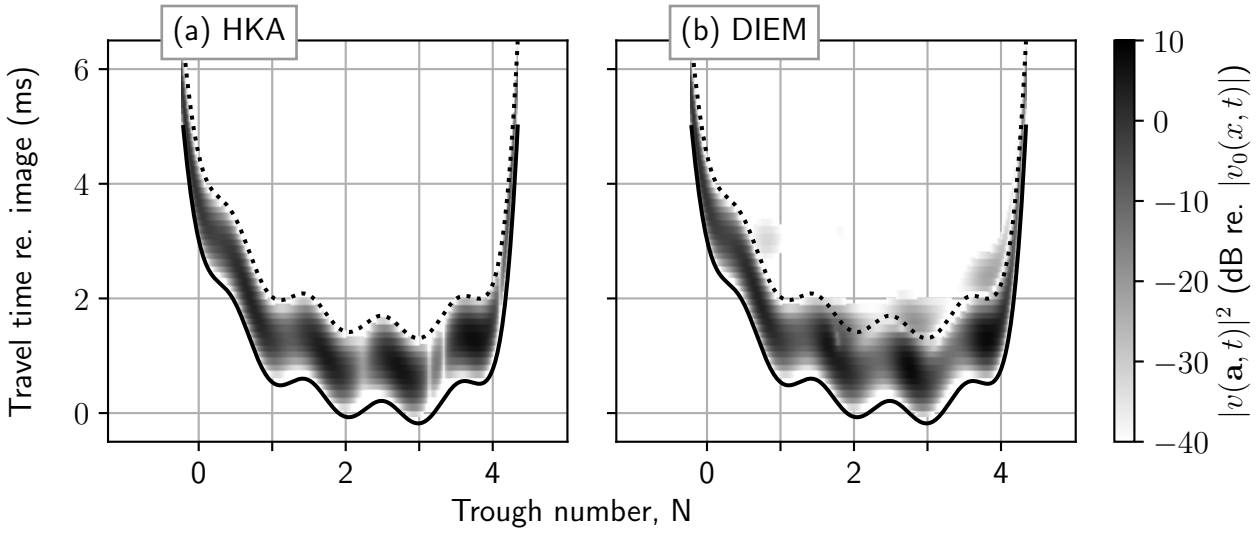

Figure 3.8: Envelope of Green's theorem integrand, $v(\mathbf{a},t)$, Eq. (3.18): (a) HKA and (b) DIEM. Solid and dashed black curves are the minimal travel time and the HKA prediction for the final arrival time, respectively, following Fig. 3.4.

for $\partial\Phi(\mathbf{a})/\partial n$ determines that a 200 m integration length is sufficient for the HIE calculation of Eq. (3.11), which is used at all frequencies required by the DIEM.

3.5.3 Time series

The envelope of Green's theorem integrand, $v(\mathbf{a},t)$, is plotted as intensity for the HKA and DIEM in Fig. 3.8, panels (a) and (b), respectively. Both results are compared to the minimum travel time, $\tau(\mathbf{a})$, and the final HKA arrival time prediction, also shown in Fig. 3.4. The integrand in Fig. 3.8 is normalized to the envelope maximum for a flat surface, $|v_0(x)| = [4\pi\sqrt{f_c\,\tau_0(x)}]^{-1}$, where $\tau_0(x)$ is the flat surface minimum travel time (grey line in Fig. 3.4).

The HKA and DIEM solutions for $v(\mathbf{a},t)$ are similar in both magnitude and shape along the surface interval used in Green's theorem integrations. The solid black line is a lower bound on both solutions, which indicates that the DIEM solution is consistent with the minimum travel time of the test setup. However, the HKA prediction for the final arrival time, the dashed black line, does not completely describe the DIEM solution. The DIEM integrand has arrivals about 0.5 ms

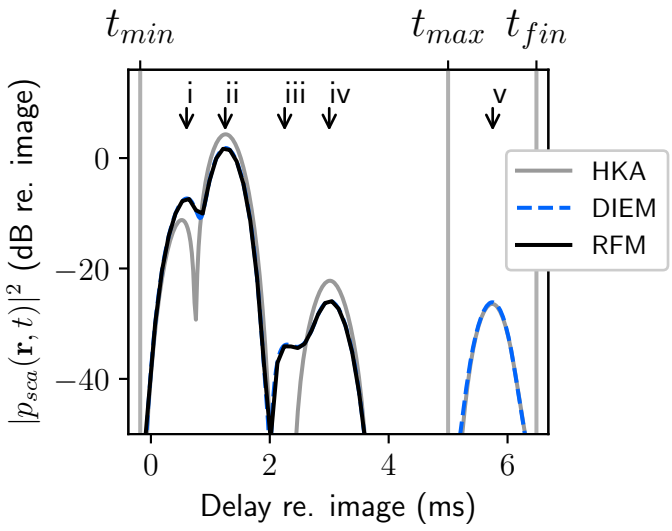

Figure 3.9: Envelope of scatter time series, $p_{sca}(\mathbf{r},t)$, for the test setup of Fig. 3.1. Distinct arrivals in DIEM time series are labeled with Roman numerals along the top of the plot. The time bounds t_{min}, t_{max} and t_{fin} are indicated along the top axis.

past the dashed black line at some surface positions, which is an indication of time extensions due to multiple scatter. However, the small amplitude and extent of $v(\mathbf{a},t)$ past the HKA final arrival time means this is not a significant change of the time domain structure of $v(\mathbf{a},t)$ from the HKA prediction. The similarity of the structure of $v(\mathbf{a},t)$ suggests that the DIEM result for $p_{sca}(\mathbf{r},t)$, calculated with the Green's theorem of Eq. (3.21), will also be similar in arrival structure to the HKA results.

The envelope of the scatter time series, $p_{sca}(\mathbf{r},t)$, is compared between the HKA, DIEM and RFM solutions in Fig. 3.9. The times of the largest arrivals, i and ii, match the eigen-ray predictions shown in Fig. 3.4 after adding the ~0.75 ms delay to reach the maximum of the transmission pulse (shown in Fig. 3.3).

Arrival iii, with the smallest amplitude, is a multiple scatter effect that is only included in the RFM and DIEM solutions. Importantly, however, while arrival iii is not predicted by the HKA, it does not extend the DIEM scatter duration past that of the HKA. This result validates the use of the HKA for predicting DIEM scatter duration for the specific test setup of Fig. 3.1, a

result predicted for general source and receiver locations by the discussion related to Fig. 3.8.

Arrival iv is a shadow zone contribution, which appears as a flattening of $\tau(\mathbf{a})$ between trough numbers 0 and 1 with no stationary points. The prediction of this arrival by the HKA indicates the advantage of numerical solution of the HKA with Eq. (3.19) over a simple stationary phase analysis.

Arrival v, apparent in HKA and DIEM solutions, is the edge arrival caused by limited spatial integrations of Green's theorem, described in Sec. 3.4.3. While time series results are calculated for a total length of t_{fin}, the valid duration of the solution is limited to t_{max}. There is negligible difference between the DIEM and RFM solutions before t_{max}, and the DIEM essentially is identical to the reference solution after the scatter IR is limited to the valid duration between t_{min} and t_{max}.

The HKA and DIEM show similar arrival structure in time, but the amplitudes of the arrivals are significantly different. The first HKA arrival, label i, is approximately 4 dB lower than the DIEM. The second and third HKA arrivals, labels ii and iv, have amplitudes about 3 dB larger than the DIEM. The distinct error between arrivals is consistent with the DIEM approaching the image solution more quickly than the HKA. The exact scatter solution at shallow grazing angles from any surface is the image solution,[20] and this limit begins to be apparent for the test setup of Fig. 3.1. The agreement of the DIEM and RFM further indicates the DIEM is an appropriate reference solution for identifying the limitations of the HKA in test setups with low grazing angle scatter.

3.6 Summary

The DIEM uses limited spatial integrations of Green's theorem to compute broadband scatter from infinite surfaces. The DIEM result is calculated as an impulse response estimate for a short time pulse transmission, which allows for a travel time description of the solution.

Importantly, the truncation error from limited spatial integrations of Green's theorem is modeled with the HKA as an arrival from the integration edges. The edge arrival model allows for separation in time between physical arrivals and the truncation error, which effectively is removed by limiting the duration of the scatter solution. A test scenario with a sinusoidal surface was used to compare the DIEM to the exact RFM scatter solution, and the DIEM matched RFM results for scatter from an infinite surface.

The DIEM determines the spatial interval in Green's theorem calculations from the arrival time of the last significant scatter arrival. Instead of computing the last significant arrival time directly, the DIEM uses an estimate made with the HKA. Comparisons of the time domain HKA and DIEM show the arrival structure of the two solutions are similar, and the HKA provides an appropriate estimate of the last scatter arrival time. The arrival structure of the HKA and DIEM is compared both at the receiver with scatter time series, and along the scattering surface with the Green's theorem integrand. The Green's theorem integrand shows that multiple scatter effects not modeled by the HKA do not significantly extend scatter time series durations, a result which largely is independent of receiver location. The DIEM therefore uses the HKA to determine the surface interval of Green's theorem integrations, at significantly less computational cost than an equivalent analysis with DIEM calculations.

Once the surface integration interval for Green's theorem is established with the HKA, the DIEM calculates the normal derivative of the pressure field on the surface, $\partial\Phi(\mathbf{a})/\partial n$. The DIEM calculation for $\partial\Phi(\mathbf{a})/\partial n$ is solved with an integral equation, which has its own spatial integration interval. A comparison between RFM and DIEM solutions for $\partial\Phi(\mathbf{a})/\partial n$ shows that a small extension of the spatial interval in Green's theorem integrations is required for the DIEM's integral equation calculations.

Although a number of calculations were made with the RFM reference solution to confirm DIEM results, the DIEM does not require the RFM solution in its computations. Instead, its results build from the commonly used HKA, and many of its results are described as departures

from the HKA. The general formulation of the DIEM, and its similarity to the HKA, serve to establish it as a viable reference solution for future scatter studies.

3.7 Acknowledgments

Chapter 3, in full, is a reprint of a rejected submission to the Journal of the Acoustical Society of America 2019, authored by Edward L. Richards, H. C. Song and W. S. Hodgkiss. The dissertation/thesis author was the primary investigator and author of this paper. While this work was not considered sufficently novel for publication as is, it represented a signifcant research effort and is included as a thesis chapter. This research was supported by the Office of Naval Research under grant N00014-18-1-2123.

Bibliography

[1] M. Siderius and M. B. Porter, "Modeling broadband ocean acoustic transmissions with time-varying sea surfaces," *The Journal of the Acoustical Society of America*, vol. 124, no. 1, pp. 137–150, 2008.

[2] M. Badiey, A. Song, and K. B. Smith, "Coherent reflection from surface gravity water waves during reciprocal acoustic transmissions," *The Journal of the Acoustical Society of America*, vol. 132, no. 4, pp. EL290–EL295, 2012.

[3] S. P. Walstead and G. B. Deane, "Intensity statistics of very high frequency sound scattered from wind-driven waves," *The Journal of the Acoustical Society of America*, vol. 139, no. 5, pp. 2784–2796, 2016.

[4] E. I. Thorsos and D. R. Jackson, "Studies of scattering theory using numerical methods," *Waves in Random Media*, vol. 1, no. 3, pp. S165–S190, 1991.

[5] E. L. Richards, H. C. Song, and W. S. Hodgkiss, "Acoustic scattering comparison of kirchhoff approximation to rayleigh-fourier method for sinusoidal surface waves at low grazing angles," *The Journal of the Acoustical Society of America*, vol. 144, no. 3, pp. 1269–1278, 2018.

[6] R. T. Marchand and G. S. Brown, "On the use of finite surfaces in the numerical prediction of rough surface scattering," *IEEE Transactions on Antennas and Propagation*, vol. 47, no. 4, pp. 600–604, 1999.

[7] E. I. Thorsos, "The validity of the Kirchhoff approximation for rough surface scattering using a Gaussian roughness spectrum," *The Journal of the Acoustical Society of America*, vol. 83, no. 1, pp. 78–92, 1988.

[8] T. W. Dawson and J. A. Fawcett, "A boundary integral equation method for acoustic scattering in a waveguide with nonplanar surfaces," *The Journal of the Acoustical Society of America*, vol. 87, no. 3, pp. 1110–1125, 1990.

[9] K. Williams, J. Stroud, and P. Marston, "High-frequency forward scattering from Gaussian spectrum, pressure release, corrugated surfaces. I. Catastrophe theory modeling," *The Journal of the Acoustical Society of America*, vol. 96, no. 3, pp. 1687–1702, 1994.

[10] P. M. van den Berg, "Reflection by a grating: Rayleigh methods," *J. Opt. Soc. Am.*, vol. 71, pp. 1224–1229, Oct 1981.

[11] R. Petit, L. Botten, M. Cadilhac, G. Derrick, D. Maystre, R. McPhedran, M. Neviere, and P. Vincent, *Electromagnetic Theory of Gratings*. Topics in Current Physics, Springer Berlin Heidelberg, 1980.

[12] W. C. Meecham, "On the use of the Kirchhoff approximation for the solution of reflection problems," *Journal of Rational Mechanics and Analysis*, vol. 5, no. 2, pp. 323–334, 1956.

[13] J. A. DeSanto, "Exact boundary integral equations for scattering of scalar waves from perfectly reflecting infinite rough surfaces," *Wave Motion*, vol. 45, no. 7, pp. 918 – 926, 2008.

[14] R. F. Millar, "The Rayleigh hypothesis and a related least-squares solution to scattering problems for periodic surfaces and other scatterers," *Radio Science*, vol. 8, no. 8-9, pp. 785–796, 1973.

[15] J. Kaiser and R. Schafer, "On the use of the I0-sinh window for spectrum analysis," *IEEE Transactions on Acoustics, Speech, and Signal Processing*, vol. 28, pp. 105–107, February 1980.

[16] F. Jensen, W. Kuperman, M. Porter, and H. Schmidt, *Computational Ocean Acoustics*. Springer, New York, NY, 2011.

[17] E. Liszka and J. McCoy, "Scattering at a rough boundary – extensions of the Kirchhoff approximation," *The Journal of the Acoustical Society of America*, vol. 71, no. 5, pp. 1093–1100, 1982.

[18] D. F. McCammon and S. T. McDaniel, "Application of a new theoretical treatment to an old problem; sinusoidal pressure release boundary scattering," *The Journal of the Acoustical Society of America*, vol. 78, no. 1, pp. 149–156, 1985.

[19] D. Holliday, L. L. DeRaad, and G. J. St-Cyr, "Volterra approximation for low grazing angle shadowing on smooth ocean-like surfaces," *IEEE Transactions on Antennas and Propagation*, vol. 43, pp. 1199–1206, Nov 1995.

[20] P. Beckmann and A. Spizzichino, "The scattering of electromagnetic waves from rough surfaces," *Norwood, MA, Artech House, Inc., 1987, 511 p.*, 1987.

Chapter 4

Observations of scatter from surface reflectors with Doppler sensitive probe signals

Previous analysis of sea-surface scatter from the KAM11 experiment focused mainly on the late-arriving striation patterns in time-varying channel impulse responses. This paper reveals additional striations in the opposite direction using Doppler-sensitive waveforms. A surface reflector model is proposed that illustrates observed Doppler shifts and relates scatter observations to positions on the sea surface.

4.1 Introduction

Studies of deterministic acoustic scatter from the sea surface describe the transient acoustic arrivals that reflect from identifiable surface features. [1] These studies are important because transient arrivals can both be predicted from, [2] and invert for, [3, 4, 5] the sea surface profile. Many of these deterministic surface scatter studies have been made in wave tanks or at relatively short ranges at-sea, and focus on completely describing observed scatter. In contrast, longer range measurements made during the Kauai Acomms MURI 2011 experiment (KAM11) had more cluttered scatter arrivals, and studies of this data have focused on describing only the striation features apparent at late delays. [6, 7, 8]

The KAM11 striations were most apparent in transmissions between two sea-floor mounted tripods and a ship-deployed receiver, shown schematically in Fig. 4.1 (a) and (b). Each transmission is labeled by tripod station, Sta07 or Sta05, and measurements discussed here were taken within 20 minutes on J191 (July 10). Following previous studies,[8, 6, 7] the single surface interaction paths in impulse response measurements are shown in Fig. 4.1 (c) and (d) for a linear frequency modulated (LFM) probe signal. The geometries for both transmissions are similar but the surface wave propagation direction is different, approximately (1) in-line or (2) opposite the acoustic propagation for Sta07 and Sta05, respectively. Most apparent after the cluttered first 4 ms of delay in Fig. 4.1 (c) and (d), striation patterns have negative or positive slope for Sta07 and Sta05, respectively.

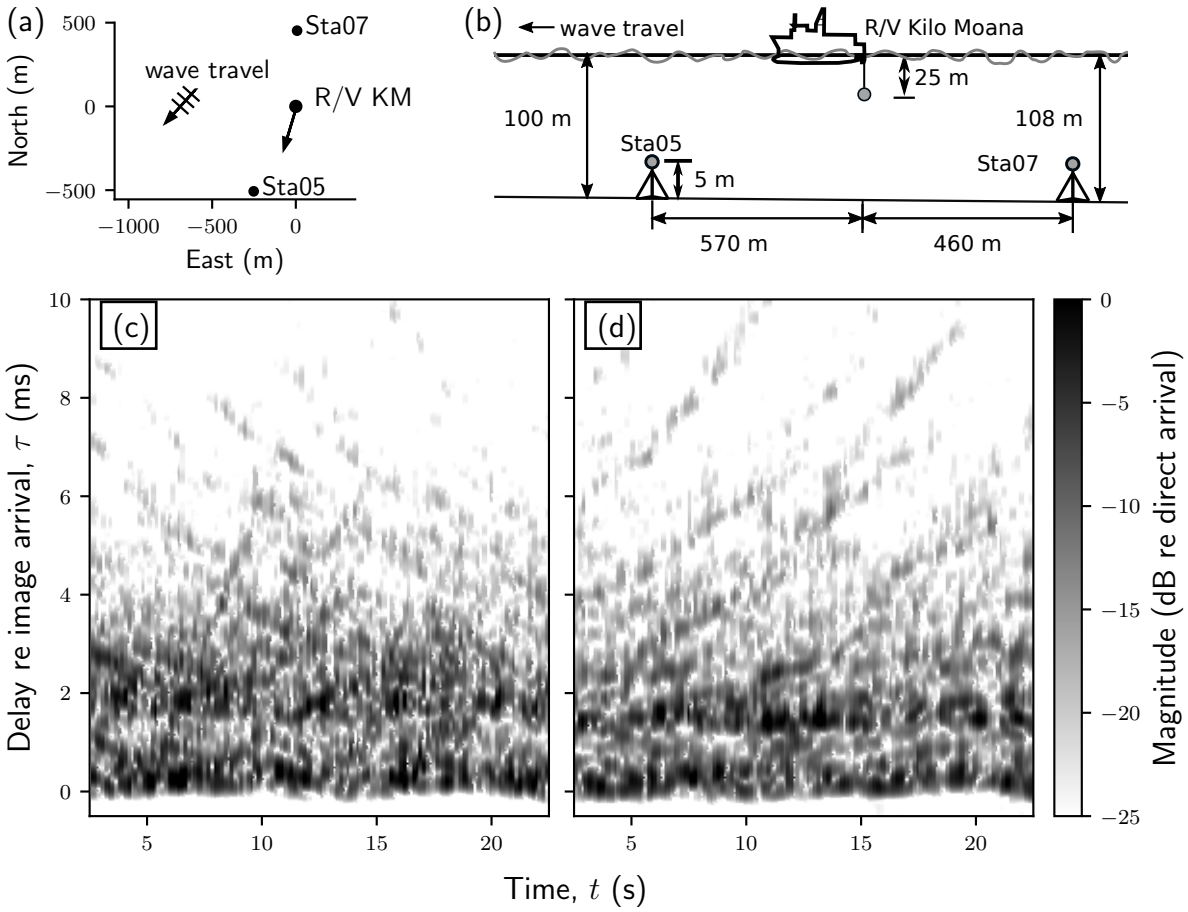

Figure 4.1: Schematic of KAM11 tripod transmissions: (a) top view, (b) side view. Transmissions were made from tripod mounted acoustic sources, and recorded on a ship deployed hydrophone. LFM impulse response estimates: (c) Sta07 (J191 23:06 UTC), (d) Sta05 (J191 23:12 UTC). Type I striations are most apparent after 4 ms delay with negative and positive slopes in panels (c) and (d), respectively.

Observed striation patterns for both transmission geometries were simulated with eigenray models for both sinusoidal and rough sea surfaces. [8, 7] The sinusoidal surface study of Choo, Seong and Song [8] demonstrated that the late-delay striation patterns are the result of reflections from the sloped surface wave face, and the striations in Fig. 4.1 (c) and (d) arise from surface reflections near the tripod sources. These striation patterns are termed Type I here. Additionally, a second set of striation patterns, termed Type II here, was predicted to arise from the surface reflections near the ship-deployed receiver. Type II striations have an opposite slope direction from Type I striations and end at earlier delays. While suggestions of the Type II striations are sometimes apparent, for example between 4-6 ms delay and 7-15 s time in Fig. 4.1 (c), observation of these features is challenging due to early delay clutter. [8]

This study uses impulse response estimates made with Doppler sensitive maximum length sequence (MLS) probe signals to reduce early delay clutter, which allows the resolution of Type II striations. Observed striation patterns are associated with surface reflectors in Sec. 4.3, and these reflectors are specified by an in-plane position and velocity. Similar to arrivals from moving targets in bistatic geometries, [9] both the magnitude and sign of the Doppler shift depends on the in-plane position of the surface reflector as well as its velocity. Section 4.4.1 demonstrates the existence of both Type I and II striations at significantly different Doppler shifts for Sta07, differences that are related to surface reflectors with similar in-plane velocities at different locations. A similar analysis of Sta05 measurements did not reveal any Type II striations, an absence related to the research vessel interfering with portions of the surface reflected path.

4.2 Estimation of time-varying surface impulse responses

In this study, impulse response estimates were made from LFM and MLS probe transmissions, centered at 10 kHz with 6 kHz bandwidth, with the two sea-floor tripods alternating transmission sequences every 2 minutes. [6] The LFM transmission was 48 ms long and repeated

every 144 ms for 40 s. The MLS transmission was 127.75 ms long and repeated without interruption for 20 s. Time-varying impulse responses are estimated for each probe signal following Choo, Seong and Song [8]

The near bottom source deployment resulted in a bottom-surface path with similar delay to the shorter surface path. Both specular arrival times appear as dark horizontal bands in Fig. 4.1 (c) and (d). For specular reflection, the delay difference between these paths is 1.8 and 1.4 ms for Sta07 and Sta05, respectively. Similar to Funk and Williams,[10] this study assumes that the same scatter event on the surface produces arrivals for both paths. Each scatter event then produces a pair of striations, separated approximately by their specular reflection delay. For Fig. 4.1 (c) and (d), however, striations cannot be attributed clearly to either the surface or surface-bottom path due to the difficulty of identifying striation pairs among the numerous arrivals.

Instead of further analyzing the busy arrival structure of the LFM impulse response estimates, this study focuses on the less cluttered MLS estimates. In contrast with the LFM, the matched filter template of the MLS selects for Doppler shift, which removes many scatter arrivals from each impulse response estimate. Each matched filter template used here is made with five repeated MLS sequences, for an approximate 0.6 ms template duration and a reciprocal Doppler resolution of 1.6 Hz.

4.3 Estimation of surface reflector position and velocity

The observed delay and Doppler shift of surface striations fit the in-plane position and velocity of a surface reflector. While this study does not explicitly describe the features on the sea surface that act as reflectors, it assumes that they are stationary points of the Helmholtz-Kirchhoff integral, following Funk and Williams.[10] The Helmholtz-Kirchhoff integral is not evaluated for any specific surface profile. Instead, the surface reflectors are assumed to be small elevation perturbations that do not change the delay significantly from the flat surface.

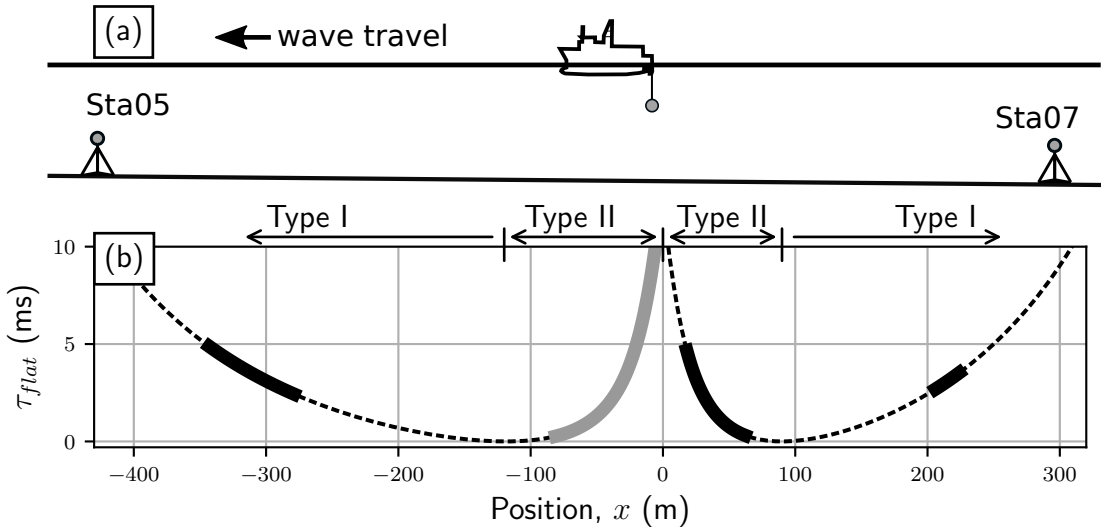

Figure 4.2: Surface reflector delay for both KAM11 tripods: (a) experimental schematic indicating vessel heading and wave travel direction, (b) delay for Sta05 and Sta07 at negative and positive x, respectively. In panel (b), the delay of a surface reflector assumes a flat surface following Eq. (4.3), and the regions associated with each striation type are indicated along the top. The in-plane positions of striations shown in Figs. 4.3 and 4.4 are drawn as thick black lines, while the region of research vessel interference is drawn as a thick grey line on the Sta05 delay curve.

The in-plane velocity of the surface reflector, $\partial x/\partial t$, is first related to a slope in the time-varying impulse response,

$$m = \frac{\partial \tau}{\partial t} = \frac{\partial \tau}{\partial x}\frac{\partial x}{\partial t}. \tag{4.1}$$

The value of m is expected to be time-varying for the curved striation patterns predicted from eigen-ray studies. [8, 7] The value of m in Eq. (4.1) determines the Doppler shift of the received signal, Δf,

$$\Delta f = -m\, f_c, \tag{4.2}$$

where f_c is the acoustic center frequency of the transmission.

The delay to a position on the surface, τ, and the spatial derivative, $\partial\tau/\partial x$, are modeled for a reflector moving along the flat surface,

$$\tau(x) \approx \frac{\sqrt{x^2 + z_{rcr}^2} + \sqrt{(x_{src} - x)^2 + z_{src}^2}}{c} - \tau_{flat}, \tag{4.3}$$

where the subscripts *src* and *rcr* indicate the source and receiver, respectively. The delay is relative to the flat surface ray, τ_{flat}, the x-axis to the hydrophone position, and the z-axis to the mean water level. The sound speed value, c =1535 m/s, is representative of the approximately 60 m deep mixed layer,[6] although delay corrections are possible for the refracting medium. [11]

The in-plane position and velocity of surface reflectors are estimated from striation delay, τ, with the inverse of Eq. 4.3. For the delay curve of either source, shown in Fig. 4.2 (b), values of τ other than zero have two possible x-positions on either side of the delay minimum. The different x-positions are in separate regions associated with each striation type, defined by the sign of $\partial\tau/\partial x$ and shown on the top of Fig. 4.2 (b). The Type I and II regions have different directions of striation slope for the same direction of surface reflector travel through Eq. (4.3). This also is illustrated using eigen-rays by Choo, Seong and Song,[8] where Regions 1 and 2 in their Fig. 4 correspond to the Type I and II regions here. The direction of the striation slope then resolves region type, and thus the in-plane position ambiguity, necessary to estimate x from τ with Eq. 4.3. Finally, a constant in-plane velocity, $\partial x/\partial t$, is chosen by eye to fit the time evolving delay of the striation pattern.

4.4 Analysis of striation patterns

The two transmission periods presented here were chosen to cover a large range of observed in-plane scatter positions, shown as the thick black lines in Fig. 4.2 (b). For both Sta07 and Sta05, Doppler shift magnitudes of 2.5 and 4.0 Hz are used to show Type I and II striations, respectively. The Type I striation Doppler shift was chosen to best capture the striations for both station transmissions. The Type II striation Doppler shift was selected by considering only Sta07 transmissions because these striations did not appear in Sta05 transmissions, discussed in Sec. 4.4.2. These values are considered representative of each striation type, and a survey of other candidate Doppler shifts did not show any additional striations.

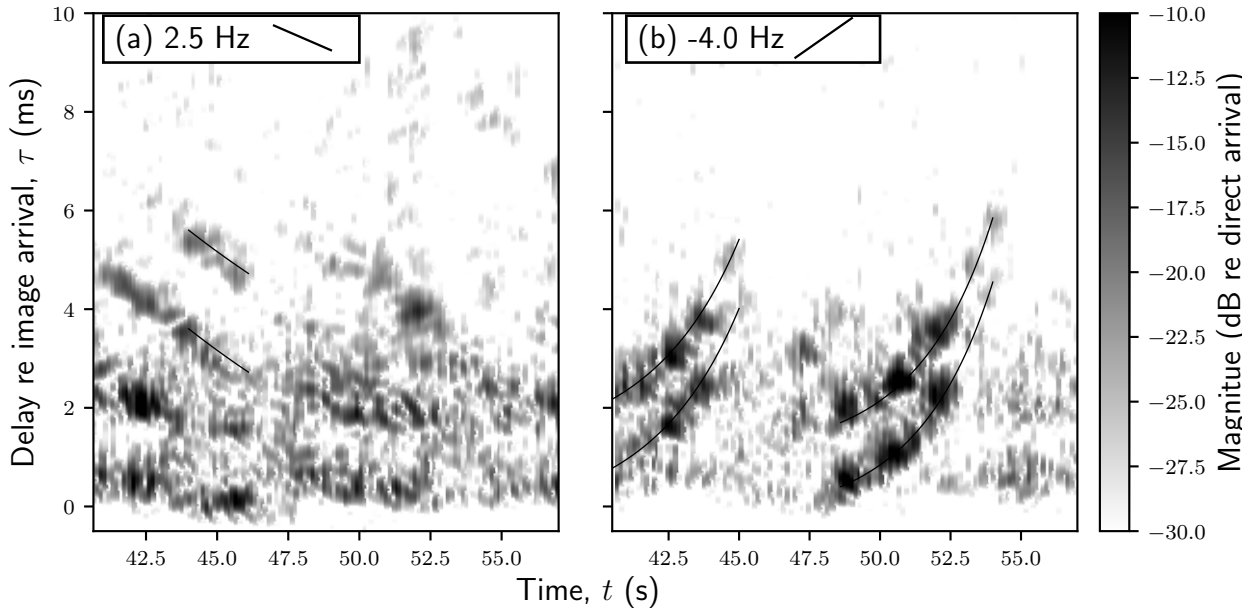

Figure 4.3: Station 07 surface impulse response estimates for the MLS probe signal (J191 23:10 UTC): (a) Type I, (b) Type II striations. Sloped line in panel labels shows maximum Doppler sensitivity. The traced arrival pair in (a) has a horizontal velocity of 8.5 m/s. The traced arrival pairs in (b) both have a horizontal velocity of 6 m/s.

4.4.1 Station 07

Doppler sensitive MLS probe signals successfully remove clutter at early delays in surface interacting paths, showing Type I and II striations in the Sta07 transmission, Fig. 4.3 (a) and (b), respectively. Type I striations are less sloped and approximately linear, while Type II striations are more sloped and curvilinear. Type II striations are more sloped because the delay curve, at positive x in Fig. 4.2 (b), is steeper for this striation type. The curvilinear shape of Type II striations is well modeled with a constant surface reflector velocity, $\partial x/\partial t$ in Eq. 4.1, because the derivative of the delay curve, $\partial\tau/\partial x$, changes significantly with position at early delays. The curved shape of the Type II striations changes the slope m over time, and consequently the Doppler shift through Eq. (4.2). Despite the changes in Doppler over a striation, the resolution of each MLS template is broad enough that a single Doppler shifted template is able to show the entire striation pattern.

The single Type I striation observation fits a reflector speed of 8.5 m/s, while the Type II

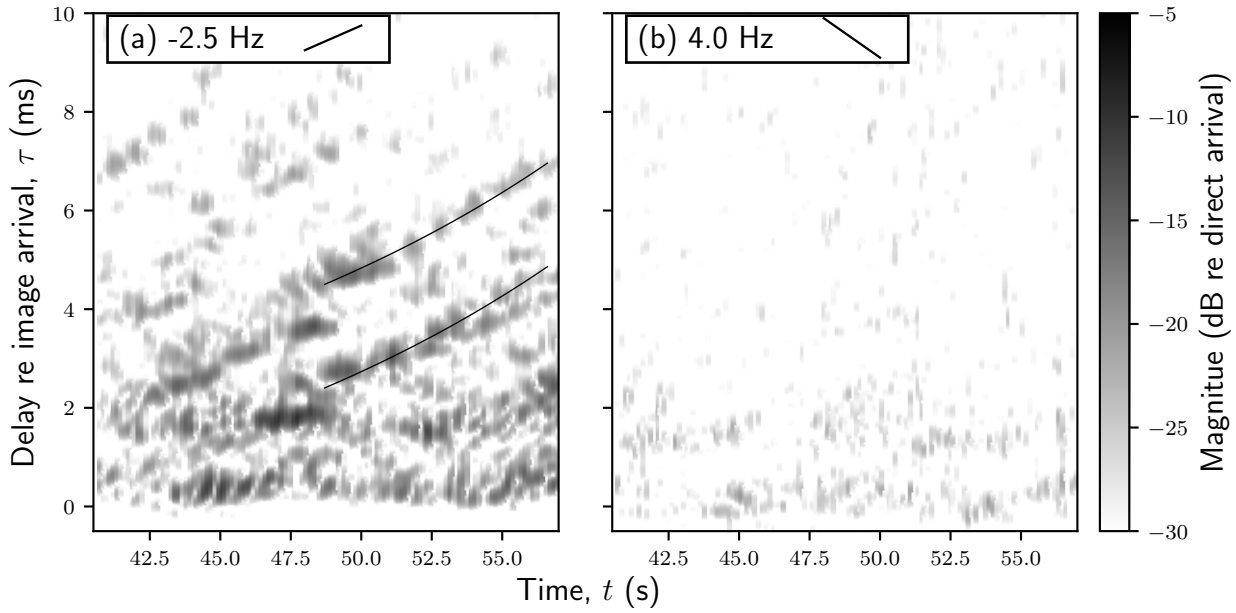

Figure 4.4: Station 05 surface impulse response estimates for the MLS probe signal (J191 22:56 UTC): (a) Type I, (b) Type II striations. Sloped line in panel labels shows maximum Doppler sensitivity. The traced arrival pair in (a) has a horizontal velocity of 8 m/s.

striations fit a lower speed of 6 m/s. The observed speeds of both striation types are consistent with the observed wave spectrum, which had a broad peak centered at a 70 m wavelength and phase speed of 10.5 m/s. [6]

4.4.2 Station 05

The MLS probe signal results for Sta05 are displayed in Fig. 4.4, for Type I and II striations in (a) and (b), respectively. A single Type I striation is fit to a reflector speed of 8 m/s, which is similar to the speed observed for the Sta07 Type I striation. The MLS impulse response estimates at the Type II striation Doppler shift show almost no energy, and no striations are apparent in Fig. 4.4 (b). While 20 s of observations cannot be considered representative of the episodic striations, a complete survey of the KAM11 Sta05 transmissions over a range of Doppler shifts did not reveal any Type II striations.

Often discussed in the context of the Helmholtz-Kirchhoff integral, [12] a possible

explanation of the absence of Type II scatter arrivals in the Sta05 observations is surface self-shadowing at low grazing angles. Although Sta05 has longer transmission paths and shallower grazing angles than Sta07, surface self-shadowing is not a sufficient explanation for the absence of Type II striations because: (1) the difference in distance between the two stations and the receiver is relatively small and (2) the Type I striation patterns are very similar for the two transmissions. Instead, it is proposed here that the hull of the R/V Kilo Moana interfered with the near receiver surface reflection paths and thus the Type II striations are not observed. The estimated region of vessel interference is shown as a thick grey line in Fig. 4.2 (b), calculated to include any path in Eq. (4.3) that passes through its draft of 7.6 m within the 57 m vessel length. The hull of the research vessel completely blocks rays in the Type II region in Fig. 4.2 (b), which explains the lack of these striations in the Sta05 observations.

4.5 Conclusion

This study used Doppler sensitive probe signals and identified two different types of striation patterns in the surface reflected paths of KAM11 time-varying impulse response estimates. Both striation types can be related to a surface reflector, characterized here by its in-plane position and velocity. These position and velocity estimates can be used in future studies as statistical descriptions of the sea-surface, or to correlate sea-surface profile measurements with acoustic scattering events. Finally, the presence of the R/V Kilo Moana was related to the lack of Type II striation observations for Sta05 measurements, providing a demonstration that a specific surface region is related to each striation type.

4.6 Acknowledgments

Chapter 4, in full, has been submitted for publication in the Journal of the Acoustical Society of Americal as an express letter, authored by Edward L. Richards, H. C. Song and W. S. Hodgkiss. The dissertation/thesis author was the primary investigator and author of this paper. This research was supported by the Office of Naval Research under grant N00014-19-1-2635.

Bibliography

[1] G. B. Deane, J. C. Preisig, C. T. Tindle, A. Lavery, and M. D. Stokes, "Deterministic forward scatter from surface gravity waves," *The Journal of the Acoustical Society of America*, vol. 132, no. 6, pp. 3673–3686, 2012.

[2] J. C. Preisig and G. B. Deane, "Surface wave focusing and acoustic communications in the surf zone," *The Journal of the Acoustical Society of America*, vol. 116, no. 4, pp. 2067–2080, 2004.

[3] S. P. Walstead and G. B. Deane, "Reconstructing surface wave profiles from reflected acoustic pulses," *The Journal of the Acoustical Society of America*, vol. 133, no. 5, pp. 2597–2611, 2013.

[4] S. P. Walstead and G. B. Deane, "Reconstructing surface wave profiles from reflected acoustic pulses using multiple receivers," *The Journal of the Acoustical Society of America*, vol. 136, no. 2, pp. 604–613, 2014.

[5] S. P. Walstead and G. B. Deane, "Determination of ocean surface wave shape from forward scattered sound," *The Journal of the Acoustical Society of America*, vol. 140, no. 2, pp. 787–797, 2016.

[6] M. Badiey, A. Song, and K. B. Smith, "Coherent reflection from surface gravity water waves during reciprocal acoustic transmissions," *The Journal of the Acoustical Society of America*, vol. 132, no. 4, pp. EL290–EL295, 2012.

[7] M. Badiey, J. Eickmeier, and A. Song, "Arrival-time fluctuations of coherent reflections from surface gravity water waves," *The Journal of the Acoustical Society of America*, vol. 135, no. 5, pp. EL226–EL231, 2014.

[8] Y. Choo, W. Seong, and H. Song, "Emergence of striation patterns in acoustic signals reflected from dynamic surface waves," *The Journal of the Acoustical Society of America*, vol. 136, no. 3, pp. 1046–1053, 2014.

[9] F. Dommermuth, "Probabilistic modelling of bistatic doppler shift," *IEE Proceedings-Radar, Sonar and Navigation*, vol. 148, no. 6, pp. 348–352, 2001.

[10] D. E. Funk and K. L. Williams, "A physically motivated simulation technique for high-frequency forward scattering derived using specular point theory," *The Journal of the Acoustical Society of America*, vol. 91, no. 5, pp. 2606–2614, 1992.

[11] Y. Choo, H. C. Song, and W. Seong, "Time-domain Helmholtz-Kirchhoff integral for surface scattering in a refractive medium," *The Journal of the Acoustical Society of America*, vol. 141, no. 3, pp. EL267–EL273, 2017.

[12] D. Holliday, L. L. DeRaad, and G. J. St-Cyr, "Volterra approximation for low grazing angle shadowing on smooth ocean-like surfaces," *IEEE Transactions on Antennas and Propagation*, vol. 43, pp. 1199–1206, Nov 1995.

Chapter 5

Conclusion and suggestions for further research

Four numerical modeling methods and one experimental analysis technique were presented that focused on improving the interpretation of ocean acoustic scatter. By focusing on estimates of the channel impulse response, both numerical and experimental analysis described the environmental impact on broadband acoustic signals in scenarios relevant to acoustic communication systems. While significant challenges remain in reconciling numerical modeling results with experimental measurements, many important features of experimental results can be captured using numerical models. These results both provide additional methods for the analysis of current acoustic scatter studies, and suggest the design of future acoustic experiments to improve the description of acoustic scatter from the sea surface.

5.1 Summary of results

Surface scatter was described using two separate approaches. Chapters 2 and 3 presented improved numerical modeling of surface scatter and focused on the calculation of exact scatter solutions. Chapter 4 focused on the analysis of experimental scatter measurements, demonstrating how Doppler sensitive impulse response estimates can significantly reduce scatter clutter and increase the number of scatter arrival observations. Taken together, these three chapters demonstrate the ways that numerical modeling describes observations well and also show the remaining challenges to reconciling these separate approaches to studying surface scatter.

5.1.1 Chapter 2

Three different numerical methods were used to study mid-frequency (1-4 kHz) scatter from a sinusoidal surface: eigen-rays, the Kirchhoff approximation and the Rayleigh-Fourier method (RFM). In ocean acoustics, eigen-rays are the most commonly used approach of these three methods and the RFM is the only exact solution considered. The Kirchhoff approximation agrees well with the RFM results in limited horizontal ranges, while the eigen-ray solution

displays error at all ranges. This comparative study led to conclusion that using a reference scatter solution should always be a component of future studies because the Kirchhoff approximation often diverges from the exact solution in ways that are hard to predict.

Other important findings include:

- The Kirchhoff approximation and the eigen-ray solution agree with each other for portions of the surface wave cycle, but the Kirchhoff approximation is continuous as the surface wave translates in position. In contrast, the eigen-ray solution has discontinuities associated with non-physical caustics and shadow-zones.

- The Kirchhoff approximation agrees with the reference solution at small to moderate horizontal source-receiver separations. The most significant differences between these solutions appear at longer ranges as over-predictions of arrival amplitude by the Kirchhoff approximation.

- Reference solutions, like the RFM presented here, are necessary for longer-range studies that require accurate amplitude results.

5.1.2 Chapter 3

Although Ch. 2 highlighted the importance of reference scatter solutions, the RFM is difficult to generalize to more realistic ocean surfaces. The integral equation solutions for surface scatter, which are exact for general scatter surfaces, were considered to provide a reference for future studies. The limited duration integral equation method (DIEM) was introduced as a numerical method that solves these integral equations. The DIEM assumes a short duration transmission and is specifically designed for band-limited impulse response simulation. The relatively short duration of the resulting scattered time series is shown to limit the spatial integrations required in the calculation of the integral equations. The computational efficiency of the DIEM makes it a practical scatter reference solution for use in future scatter studies with more general surfaces.

Other important findings include:

- Multiple scatter effects are localized along the surface with the kernel of the integral equation. The importance of multiple scatter increases with separation between source and receiver, consistent with the accuracy of the single scatter Kirchhoff approximation at short ranges.

- While DIEM and RFM produce essentially identical results, the DIEM is more computationally efficient and therefore allows analysis of more general surfaces than the RFM.

- The sinusoidal surface was used to demonstrate the accuracy of the DIEM, but the use of more realistic sea surface profiles are necessary before comparisons can be made between at-sea experiments and numerical model predictions.

5.1.3 Chapter 4

The scatter arrivals measured in channel impulse response estimates during the KAM11 experiment were shown to have significant differences in Doppler shift. Doppler sensitive probe signals were used to select for these different Doppler shifts in impulse response estimates, significantly reducing early delay clutter. This allowed for the observation of more striation patterns than previously reported for this data set, demonstrating a range of Doppler shifts that is more consistent with predictions from previous numerical studies. Finally, the observed Doppler shifts in scatter arrivals were directly related to position and velocity estimates of a reflecting feature on the sea surface.

Other important findings include:

- While the velocity of the surface reflectors gives rise to a Doppler shift in each scattered arrival, different scattered arrivals have significantly different Doppler shifts that depend on surface reflector position.

- A constant velocity, unique to each surface reflector, matches observations well. This is true even when scatter arrivals appear as highly curved features with variable Doppler shift resulting from the bi-static experimental geometry.

- While two experimental setups were analyzed from the KAM11 experiment, only one setup showed the range of Doppler shift values expected for the scattered arrivals. The missing Doppler shifts were related to positions on the surface occupied by the research vessel collecting the acoustic recordings. The interference from the vessel hull was then related to the absence of arrivals with certain Doppler shifts observed for one experimental setup.

5.2 Suggestions for further research

The first part of this thesis, Ch. 2 and 3, described numerical results for surface scatter from a simple sinusoidal sea surface. Chapter 3 further described the DIEM solution method for surface scatter problems, which is intended for use in future scatter studies with more realistic sea surfaces. The second part of this thesis, Ch. 4, used a travel time model to analyze experimental observations made during KAM11 and described scattered arrivals as reflections from features moving along the sea surface. Taken together, these three chapters form a framework for future work to bring these two lines of inquiry together. The future work would both verify numerical modeling methods by matching results to the scatter observations, and describe the surface reflectors discussed in Ch. 4 with numerical studies.

Comparison of DIEM results with KAM11 experimental data requires future numerical studies with a one-dimensional sea surface that matches the observed wave spectrum. This comparison will inform what further model development is necessary to better match observations. Possible future model development could include effects such as: out of plane wave propagation [1], 2-D surface wave spectra, non-linear wave shapes [2], and bubble clouds. Additionally, the scatter model can be improved for more general propagation conditions by including refraction

effects [3] and interaction with the ocean bottom. These improvements to scattering modeling can be verified using available experimental results, like those from KAM11, or future experiments that simultaneously measure the instantaneous surface profile and the acoustic channel impulse response.

Future experimental studies informed by the analysis of Ch. 4 could serve to further the understanding of surface scatter in the acoustic channel. Controlled wave tank experiments at longer ranges than previous studies (i.e. [4, 5]) could clearly demonstrate the relationship between reflector position and apparent Doppler shift. Also, these results would be the first step in comparing the predictions of the Kirchhoff approximation to exact scatter solutions. The most important demonstration of both the Doppler sensitive analysis of surface scatter and the DIEM would be an at-sea experiment that measures the acoustic channel simultaneously with the ocean surface. While an at-sea experiment would add significant complexity to both modeling and data analysis, initial results indicate that limited regions of the sea surface are most significant to surface scatter. Targeted sampling of the most important portions of the surface could relate significant acoustic scatter events to moving surface wave features, and lead to better prediction of acoustic scatter from ocean wave observations.

Finally, both numerical and experimental results presented here contribute to the understanding of time-evolving surface scatter in the broadband signals most relevant to acoustic communication. The improved understanding of time-evolving surface scatter can improve acoustic communication systems by increasing the accuracy of channel simulations. Future work with these channel simulations could also be used to improve the prediction of existing communication system performance in novel environments. These results are expected to be most relevant to mid-range acoustic communication scenarios in shallow water conditions, important for applications like the growing prevalence of autonomous underwater vehicle surveys.

Bibliography

[1] Y. Choo, H. C. Song, and W. Seong, "Numerical study of three-dimensional sound reflection from corrugated surface waves," *The Journal of the Acoustical Society of America*, vol. 140, no. 4, pp. 2290–2296, 2016.

[2] M. Badiey, A. Song, and K. B. Smith, "Coherent reflection from surface gravity water waves during reciprocal acoustic transmissions," *The Journal of the Acoustical Society of America*, vol. 132, no. 4, pp. EL290–EL295, 2012.

[3] Y. Choo, H. C. Song, and W. Seong, "Time-domain Helmholtz-Kirchhoff integral for surface scattering in a refractive medium," *The Journal of the Acoustical Society of America*, vol. 141, no. 3, pp. EL267–EL273, 2017.

[4] S. P. Walstead and G. B. Deane, "Reconstructing surface wave profiles from reflected acoustic pulses," *The Journal of the Acoustical Society of America*, vol. 133, no. 5, pp. 2597–2611, 2013.

[5] S. P. Walstead and G. B. Deane, "Intensity statistics of very high frequency sound scattered from wind-driven waves," *The Journal of the Acoustical Society of America*, vol. 139, no. 5, pp. 2784–2796, 2016.